

Priors with Coupled First and Second Order Differences for Manifold-Valued Image Processing

Ronny Bergmann · Jan Henrik Fitschen · Johannes Persch · Gabriele Steidl

June 14, 2018

Abstract We generalize discrete variational models involving the infimal convolution (IC) of first and second order differences and the total generalized variation (TGV) to manifold-valued images. We propose both extrinsic and intrinsic approaches. The extrinsic models are based on embedding the manifold into an Euclidean space of higher dimension with manifold constraints. An alternating direction methods of multipliers can be employed for finding the minimizers. However, the components within the extrinsic IC or TGV decompositions live in the embedding space which makes their interpretation difficult. Therefore we investigate two intrinsic approaches: for Lie groups, we employ the group action within the models; for more general manifolds our IC model is based on recently developed absolute second order differences on manifolds, while our TGV approach uses an approximation of the parallel transport by the pole ladder. For computing the minimizers of the intrinsic models we apply gradient descent algorithms. Numerical examples demonstrate that our approaches work well for certain manifolds.

Keywords Infimal convolution, total generalized variation, higher order differences, manifold-valued images, optimization on manifolds

Ronny Bergmann · Jan Henrik Fitschen · Johannes Persch · Gabriele Steidl

Departement of Mathematics, Technische Universität Kaiserslautern, Paul-Ehrlich-Str. 31, 67663 Kaiserslautern, Germany

E-mail: bergmann@mathematik.uni-kl.de,

E-mail: fitschen@mathematik.uni-kl.de,

E-mail: persch@mathematik.uni-kl.de,

E-mail: steidl@mathematik.uni-kl.de.

Gabriele Steidl

Fraunhofer ITWM, Kaiserslautern, Germany

E-mail: steidl@mathematik.uni-kl.de.

Mathematics Subject Classification (2000)

49M15, 49M25, 49Q20, 68U10, 56Y99

1 Introduction

Variational models of the form

$$\mathcal{E}(u) = \mathcal{E}_{\text{data}}(u; f) + \alpha \mathcal{E}_{\text{prior}}(u), \quad \alpha > 0,$$

where f is the given data set, $\mathcal{E}_{\text{data}}$ the data fitting term and $\mathcal{E}_{\text{prior}}$ the prior also known as regularization term, were applied for various tasks in image processing. In this paper, we restrict our attention to least squares data fitting terms.

Starting with methods having first order derivatives in their prior like the total variation (TV) [58], higher order derivatives were incorporated into the prior to cope with the staircasing effect caused by the TV regularization and to better adapt to specific applications. Besides additive coupling of higher order derivatives, see, e.g., [50], their infimal convolution (IC) [26] or the total generalized variation (TGV) [21] were proposed in the literature. In many applications such as image denoising IC [60, 61] or TGV [19, 21, 23] show better results than just the additive coupling. For discrete TGV versions we refer to [60, 61]. A preconditioned Douglas–Rachford algorithm can be used to efficiently compute the minimizer of the TGV penalized problem [22]. An extension of TGV to vector-valued images with applications in color image restoration was given in [18]. In [9, 10], IC, resp. TGV, of motion fields were successfully applied to strain analysis, in particular for the early detection of cracks in materials during tensile tests.

With the emerging possibilities to capture different modalities of data, image processing methods are transferred to the case where the measurements (pixels) take

values on Riemannian manifolds. Examples are Interferometric Synthetic Aperture Radar (InSAR) [11, 25] with values on the circle \mathbb{S}^1 , directional data on the 2-sphere \mathbb{S}^2 , electron backscatter diffraction (EBSD) [8, 39] with data on quotient manifolds of $\text{SO}(3)$ or diffusion tensor magnetic resonance imaging (DT-MRI) [31], where each measurement is a symmetric positive definite 3×3 matrix. These are rather simple manifolds for which explicit expressions of their geodesic distance and exponential map are known.

Recently, the discrete TV model has been generalized to Riemannian manifolds in an intrinsic way [46, 63, 67]. Note that finding a global minimizer of the optimization problem is NP hard already for the case of the circle $\mathcal{M} = \mathbb{S}^1$ [27, 30]. In [6, 16, 17], the model was extended to include second order differences, where the coupling of the first and second order differences was only realized in an additive manner. The approach is based on a proper generalization of absolute values of second order differences to the manifold-valued setting. For the special case of DT-MRI, i.e., symmetric positive definite matrices of size 3×3 , another approach using tensor calculus resulting in the Frobenius norm instead of a distance on the Riemannian manifold was investigated in [62] and extended to a TGV approach in [65]. Numerical analysis for \mathbb{S}^2 -valued functions was also established in [2].

In this paper, we generalize discrete variational models with least squares data term and IC, resp. TGV prior to the manifold-valued setting. We derive extrinsic and intrinsic approaches. The extrinsic models which generalize the first order model in [55, 56] have the drawback that the decomposition components of IC and TGV live in the higher dimensional embedding space which makes their interpretation difficult. Therefore we propose two intrinsic approaches. For Lie groups as the circle \mathbb{S}^1 or the special orthogonal group $\text{SO}(3)$, we incorporate the group operation within the IC and TGV models which lead to decompositions within the manifold. For more general Riemannian manifolds, our so-called Midpoint IC approach relies on the generalization of the absolute value of the second order difference by the distance of its center point from a geodesic joining the two other points [6]. Our TGV model is based on the approximation of the parallel transport by the pole ladder [47]. Note that the pole ladder mimics the parallel transport exactly for symmetric Riemannian manifolds all our numerical examples belong to. It leads to a decomposition within the tangent bundle of the manifold. We acknowledge, that in parallel to our work an axiomatic TGV model for manifold-valued images was developed by Bredies et al. [20] which was only available for the revised version of this manuscript.

The first version of our paper contained an extrinsic TGV approach, a TGV approach for Lie groups as well as a remark on an intrinsic approach by the Schild's ladder. This remark was extended in the final version, where we replaced the Schild's ladder by the Pole ladder, since the later one is an exact scheme for parallel transport in symmetric spaces. However, our approach is different from those in [20]. As suggested in our original remark, we work on the tangent bundle, while they work on the manifold itself. In contrast to our isotropic model, the authors in [20] propose an anisotropic one using parallel transport or its approximation by Schild's ladder. Moreover, they focus on a cyclic proximal point algorithm, while we derive a gradient descent method. For more details see Remark 5.1.

In the extrinsic case we choose an alternating direction method of multipliers (ADMM) for finding a (local) minimizer of the functionals. For the intrinsic models we smooth the functionals so that a gradient descent algorithm can be applied.

Various numerical examples show the denoising potential for images with values on the

- spheres \mathbb{S}^d , $d = 1, 2$, which includes the important case of cyclic (phase) data;
- special orthogonal group $\text{SO}(3)$;
- symmetric positive definite $r \times r$ matrices $\mathcal{P}(r)$.

The explicit expressions required for our computations are given in the Appendix B. The first two kind of manifolds are compact, while $\mathcal{P}(r)$ is an open convex cone in $\mathbb{R}^{r,r}$.

We developed the extrinsic IC model and the Midpoint IC approach for manifold-valued images in the SSVM conference paper [13] and were invited to submit a full journal paper to JMIV. The current paper extends the SSVM paper significantly by models for Lie groups as well as all extrinsic and intrinsic TGV approaches.

The outline of the paper is as follows: In Section 2, we recall the discrete variational models for denoising gray-values images which we want to generalize. In Section 3, we propose the extrinsic models and comment how the ADMM algorithm can be adapted to these models. Unfortunately, dealing with manifolds requires to install certain preliminaries. This is briefly done in Section 4 and maybe skipped if the reader is familiar with the notation on manifolds. We propose an intrinsic Midpoint IC model and a TGV model based on the pole ladder in Section 5. In Section 6, we follow another idea driven by the group operation to set up intrinsic models for Lie groups. Section 7, shows how minimizers of the (smoothed) intrinsic models can be computed via a gradient descent algorithms and provides the necessary gradients. Numerical examples are presented in

Section 8. The paper finishes with conclusions in Section 9. Various technical details for the computation on manifolds are postponed to the appendix.

2 Models for Real-Valued Images

In this section, we briefly reconsider models with priors containing first and second order differences for gray-value images, where the focus is on the coupling of first and second order terms. To keep the technicalities simple, we just rely on gray-value images, but the approach can be simply generalized to images with values in an Euclidean space as, e.g., RGB images.

Let

$$\Gamma := \{1, \dots, N_1\} \times \{1, \dots, N_2\}$$

denote the pixel grid of an image of size $N_1 \times N_2$ and $N := N_1 N_2$. We address grid points by $i = (i_1, i_2)$. Let $u: \Gamma \rightarrow \mathbb{R}$ be a gray-value image. As data fitting term we focus on

$$\mathcal{E}_{\text{data}}(u; f) := \frac{1}{2} \|f - u\|_2^2, \quad (2.1)$$

where the images are considered columnwise reshaped into vectors.

To set up the different priors we need first and second order differences. By $D_x u$ we denote the forward differences in x -direction with Neumann (mirror) boundary conditions

$$(D_x u)_i := \begin{cases} u_{i+(1,0)} - u_i & \text{if } i + (1,0) \in \Gamma, \\ 0 & \text{otherwise,} \end{cases}$$

and analogously in y -direction. Then

$$\nabla := \begin{pmatrix} D_x \\ D_y \end{pmatrix}$$

serves as discrete gradient and $\nabla u: \Gamma \rightarrow \mathbb{R}^2$. For mappings $\xi: \Gamma \rightarrow \mathbb{R}^s$ we introduce the mixed norm

$$\|\xi\|_{2,1} := \sum_{i \in \Gamma} |\xi_i|, \quad |\xi_i| := (\xi_{i,1}^2 + \dots + \xi_{i,s}^2)^{\frac{1}{2}}. \quad (2.2)$$

We define the discrete TV regularizer by

$$\text{TV}(u) := \|\nabla u\|_{2,1} = \sum_{i \in \Gamma} \left(\sum_{j \in \mathcal{N}(i)} |u_j - u_i|^2 \right)^{\frac{1}{2}}, \quad (2.3)$$

where $\mathcal{N}(i) := \{i + (0,1), i + (1,0)\} \cap \Gamma$ denotes the forward neighbors of pixel $i \in \Gamma$. The backward difference $\tilde{D}_x u$ in x -direction is given by

$$(\tilde{D}_x u)_i := \begin{cases} u_i - u_{i-(1,0)} & \text{if } i \pm (1,0) \in \Gamma, \\ 0 & \text{otherwise,} \end{cases}$$

and similarly in y -direction. The choice of zero at the right boundary of the backward difference becomes clear in (2). We will apply backward differences to vectors $\xi: \Gamma \rightarrow \mathbb{R}^2$ in two forms

$$\tilde{\nabla} := \begin{pmatrix} \tilde{D}_x & 0 \\ \tilde{D}_y & 0 \\ 0 & \tilde{D}_x \\ 0 & \tilde{D}_y \end{pmatrix}, \quad \tilde{\nabla}_S := \begin{pmatrix} \tilde{D}_x & 0 \\ \frac{1}{2} \tilde{D}_y & \frac{1}{2} \tilde{D}_x \\ 0 & \tilde{D}_y \end{pmatrix}.$$

We define central second order differences in x -direction

$$D_{xx} := \tilde{D}_x D_x,$$

i.e.,

$$(D_{xx} u)_i := \begin{cases} u_{i-(1,0)} - 2u_i + u_{i+(1,0)} & \text{if } i \pm (1,0) \in \Gamma, \\ 0 & \text{otherwise,} \end{cases}$$

and mixed second order differences

$$D_{xy} := \tilde{D}_y D_x,$$

and analogously for the other directions. Then a TV_2 regularizer can be defined by the Frobenius norm of the Hessian of u ,

$$\begin{aligned} \text{TV}_2(u) &:= \|\tilde{\nabla} \nabla u\|_{2,1} \\ &= \sum_{i \in \Gamma} (|D_{xx} u|_i^2 + |D_{yy} u|_i^2 + |D_{xy} u|_i^2 + |D_{yx} u|_i^2)^{\frac{1}{2}}. \end{aligned} \quad (2.4)$$

The infimal convolution (IC) of two functions

$F_i: \mathbb{R}^N \rightarrow \mathbb{R} \cup \{+\infty\}$, $i = 1, 2$, is defined by

$$(F_1 \square F_2)(u) := \inf_{u=v+w} \{F_1(v) + F_2(w)\}.$$

If F_i , $i = 1, 2$, are proper, convex, lower semi-continuous and $F_i(u) = F_i(-u)$, then $F_1 \square F_2$ is also proper, convex, lower semi-continuous and the infimum is attained [54, 61].

We consider two common ways to incorporate first and second order information into the prior, namely in an additive way and by IC. The corresponding priors look for $\beta \in (0, 1)$ as follows:

1. Additive Coupling

$$\text{TV}_{1 \wedge 2}(u) := \beta \text{TV}(u) + (1 - \beta) \text{TV}_2(u).$$

2. Infimal Convolution

$$\text{IC}(u) := \min_{u=v+w} \{\beta \text{TV}(v) + (1 - \beta) \text{TV}_2(w)\},$$

The IC model is related to TGV of order two given by:

3. Total Generalized Variation

$$\text{TGV}(u) := \min_{\xi} \left\{ \beta \|\nabla u - \xi\|_{2,1} + (1 - \beta) \|\tilde{\nabla}_S \xi\|_{2,1} \right\}, \quad (2.5)$$

In contrast to the IC prior, the TGV prior does not require the computation of second order differences. The relation to the IC model, which by (2) and (2) can be rewritten as

$$\text{IC}(u) = \min_w \left\{ \beta \|\nabla(u - w)\|_{2,1} + (1 - \beta) \|\tilde{\nabla} w\|_{2,1} \right\}$$

appears if $\xi: \Gamma \rightarrow \mathbb{R}^2$ in (2) has the form $\xi = \nabla w$ for some $w: \Gamma \rightarrow \mathbb{R}$. Then both models differ only in the use of the nonsymmetric or symmetric backward difference operator.

For the IC and TGV models we are interested in the corresponding decompositions:

IC Decomposition ($u = v + w$)

$$E_{\text{IC}}(v, w) := \frac{1}{2} \|f - v - w\|_2^2 + \alpha(\beta \text{TV}(v) + (1 - \beta) \text{TV}_2(w)). \quad (2.6)$$

TGV Decomposition ($\nabla u = \tilde{\xi} + \xi$)

$$E_{\text{TGV}}(u, \xi) := \frac{1}{2} \|f - u\|_2^2 + \alpha(\beta \underbrace{\|\nabla u - \xi\|_{2,1}}_{\xi} + (1 - \beta) \|\tilde{\nabla} \xi\|_{2,1}).$$

For details on the discrete models we refer to [61]. In various applications, the individual IC components v and w are of interest, e.g., in motion separation [40] or early detection of cracks in materials during tensile tests [9, 10]. In the Euclidean setting, tools from convex analysis can be applied for finding minimizers of the functionals including algorithms based on duality theory as the ADMM.

3 Extrinsic Models for Manifold-Valued Images

The simplest idea to generalize the gray-value models to images $u: \Gamma \rightarrow \mathcal{M}$ having values in a manifold \mathcal{M} is to embed the manifold into an Euclidean space. Recall that by Whitney's theorem [68] every smooth d -dimensional manifold can be smoothly embedded into an Euclidean space of dimension $n = 2d$. Moreover, by Nash's theorem [49] every Riemannian manifold can be isometrically embedded into an Euclidean space of suitable dimension. Assuming that \mathcal{M} is embedded in \mathbb{R}^n , we can just apply the three Euclidean models from the previous section, which we denote by

$$\mathcal{E}_*, \quad * \in \{\text{ADD}, \text{IC}, \text{TGV}\},$$

for $u \in \mathbb{R}^{nN}$ with the constraint that the image values have to lie in the manifold. In other words, we are interested in

$$\mathcal{E}_*^{\text{ext}}(u) := \mathcal{E}_*(u) + \iota_{\mathcal{M}^N}(u), \quad * \in \{\text{ADD}, \text{IC}, \text{TGV}\},$$

and for the IC and TGV decompositions in

$$E_{\text{IC}}^{\text{ext}}(v, w) := E_{\text{IC}}(v, w) + \iota_{\mathcal{M}^N}(v + w),$$

$$E_{\text{TGV}}^{\text{ext}}(u, \xi) := E_{\text{TGV}}(u, \xi) + \iota_{\mathcal{M}^N}(u),$$

where $\iota_{\mathcal{M}^N}$ denotes the indicator function of the product manifold \mathcal{M}^N . Due to the manifold constraints, the models are in general no longer convex. Exceptions are manifolds which are closed convex sets in the embedding space as, e.g., (the closure of) $\mathcal{P}(r)$. If \mathcal{M} is closed, we directly get the existence of a global minimizer by the coercivity and lower semi-continuity of the functional. For the squared ℓ_2 -TV model an extrinsic approach was given in [55, 56] with a sketch how it can be generalized for the additive model. The extrinsic IC model was discussed in our conference paper [13].

To minimize $\mathcal{E}_{\text{ADD}}^{\text{ext}}(u)$, $E_{\text{IC}}^{\text{ext}}(v, w)$ and $E_{\text{TGV}}^{\text{ext}}(u, \xi)$ we apply an alternating direction method of multipliers (ADMM) [32, 37] in the form given in [24]. For details we refer to [52]. As additional step to the Euclidean setting ADMM requires the orthogonal projections of elements from the embedding space onto the manifold. For the manifolds in our numerical example we notice the following:

- For $\mathbb{S}^d \subset \mathbb{R}^{d+1}$, the projection is just the normalization of the vector with respect to the Euclidean norm in \mathbb{R}^{d+1} .
- For $\text{SO}(3)$, the authors of [55, 56] suggested to embed the $\text{SO}(3)$ into \mathbb{R}^9 . Then the projection requires the singular value decomposition of the matrix in $\mathbb{R}^{3,3}$ we want to project. In this paper, we prefer an embedding of $\text{SO}(3)$ into \mathbb{R}^4 via the quaternion representation, see Appendix B. This reduces the dimension of the problem and the projection is again just a normalization.
- For $\mathcal{P}(r) \subset \mathbb{R}^n$, $n = \frac{r(r+1)}{2}$, the orthogonal projection approach is in general not possible since the manifold is an *open* cone of \mathbb{R}^n . A numerical remedy would be to project onto the closed cone and add a small parameter to the eigenvalues of the resulting matrix to make it positive definite. Often also a convex barrier function as $-\log \det$ is added instead of the indicator function to stay in the manifold, see, e.g., [43]. However, in this paper, we apply only intrinsic approaches to images with values in $\mathcal{P}(r)$.

Remark 3.1 (Convergence of ADMM) If \mathcal{M} is a closed, convex set in \mathbb{R}^n , then the algorithm converges by stan-

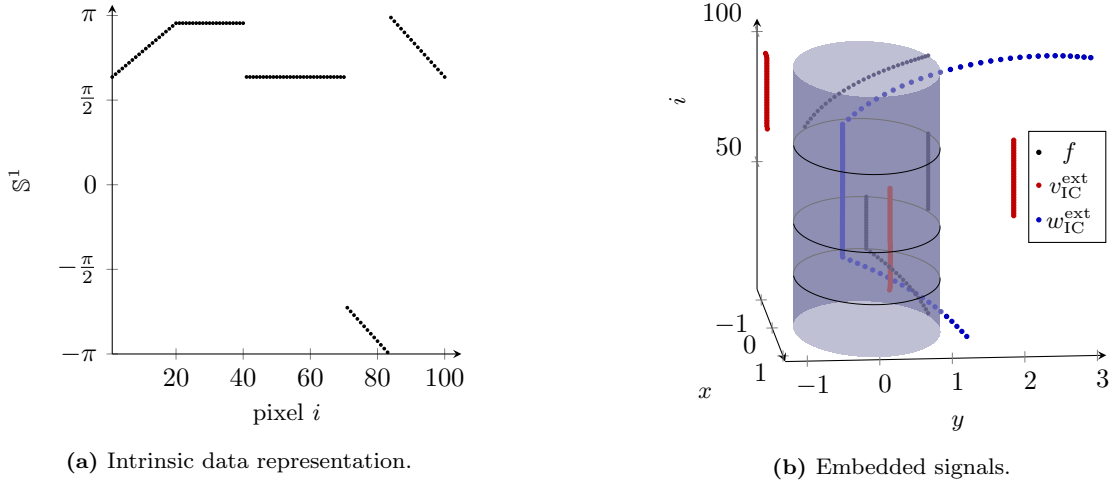


Fig. 3.1 Extrinsic IC model: Decomposition of a piecewise geodesic signal f with values in \mathbb{S}^1 . (a) Original signal f determined by its angles in $[-\pi, \pi)$. (b) Decomposition of f into its piecewise constant part $v_{\text{IC}}^{\text{ext}}$ (red) and piecewise linear part $w_{\text{IC}}^{\text{ext}}$ (blue) which can only be depicted in the embedding space \mathbb{R}^2 of \mathbb{S}^1 .

dard arguments. For spheres and the $\text{SO}(3)$, convergence is observed numerically, but cannot be guaranteed theoretically.

The convergence of the ADMM for special non-convex functionals was recently addressed in [66]. Unfortunately, the assumptions of that paper do not fit into our setting: More precisely, Assumption 2 in [66] would require with respect to our setting that the range of $(\nabla^T, I)^T$ is a subset of the range of the identity matrix which is clearly not the case.

A possibility to circumvent theoretical convergence problems would be to consider a smoothed version of the functional such that it becomes Lipschitz differentiable and a gradient reprojection algorithm can be applied. For such an algorithm convergence was shown in [4] for functions satisfying a Kurdyka-Łojasiewicz property. However, in our experiments, the algorithm shows a bad convergence behavior numerically such that we prefer ADMM. \square

The following example motivates our efforts to find intrinsic IC and TGV decompositions.

Example 3.1 We apply the extrinsic IC decomposition (2) with parameters $\alpha = 0.03$, $\beta = \frac{1}{3}$ to the phase-valued (noise-free) signal f of length $N_1 = 100$. In Fig. 3.1 (left) the signal is given by its angles in $[-\pi, \pi)$. It consists of a linearly increasing line, two constant parts divided by a small jump and a decreasing part. The second „jump“ in the signal is smaller than it occurs, since the shorter arc on the circle is the one “wrapping” around (going over $\pm\pi$). The “jump” at $t = 82$ is just only due to the representation system. Embedding each pixel $f_i \in \mathbb{S}^1$ into \mathbb{R}^2 yields the black signal in \mathbb{R}^3 shown in Fig. 3.1 (right). Since the model decomposes

$f \approx v_{\text{IC}}^{\text{ext}} + w_{\text{IC}}^{\text{ext}}$ within the embedding space \mathbb{R}^2 , the components can only be visualized within \mathbb{R}^3 , in particular not in the left plot. Still, $v_{\text{IC}}^{\text{ext}}$ is piecewise constant and contains the jumps, and $w_{\text{IC}}^{\text{ext}}$ is continuous.

4 Preliminaries on Manifolds

Let \mathcal{M} be a connected, complete d -dimensional Riemannian manifold. By $T_x\mathcal{M}$ we denote the tangent space of \mathcal{M} at $x \in \mathcal{M}$ with the Riemannian metric $\langle \cdot, \cdot \rangle_x$ and corresponding norm $\|\cdot\|_x$. Further, let $T\mathcal{M}$ be the tangent bundle of \mathcal{M} . By $\text{dist}: \mathcal{M} \times \mathcal{M} \rightarrow \mathbb{R}_{\geq 0}$ we denote the geodesic distance on \mathcal{M} . Let \mathcal{M}^N be the product or N -fold power manifold with product distance

$$\mathbf{dist}^2(x, y) := \left(\sum_{j=1}^N \text{dist}^2(x_j, y_j) \right)^{\frac{1}{2}}.$$

Let $\gamma_{x,y}: [0, 1] \rightarrow \mathcal{M}$ be a (not necessarily shortest) geodesic connecting $x, y \in \mathcal{M}$. We will also use the notation $\gamma(x, y; t) := \gamma_{x,y}(t)$ to address points on the curve. Further, we apply the notation $\gamma_{x;\xi}$ to characterize the geodesics by its starting point $\gamma_{x;\xi}(0) = x$ and direction $\dot{\gamma}_{x;\xi}(0) = \xi \in T_x\mathcal{M}$. Note that the geodesic $\gamma_{x,y}$ is unique on manifolds with nonpositive curvature. Simply connected, complete Riemannian manifolds of nonpositive sectional curvature are called Hadamard manifolds. Examples are the manifold of positive definite matrices or hyperbolic spaces. The exponential map $\exp_x: T_x\mathcal{M} \rightarrow \mathcal{M}$ is defined by

$$\exp_x(\xi) := \gamma_{x;\xi}(1).$$

Since \mathcal{M} is connected and complete, we know by the Hopf-Rinow theorem [41] that the exponential map is

indeed defined on the whole tangent space. The exponential map realizes a local diffeomorphism from a neighborhood $\mathcal{D}_T(0_x)$ of the origin 0_x of $T_x\mathcal{M}$ into a neighborhood of $x \in \mathcal{M}$. More precisely, extending the geodesic $\gamma_{x;\xi}$ from $t = 0$ to infinity is either minimizing $\text{dist}(x, \gamma_{x;\xi}(t))$ all along or up to a finite time t_0 and not any longer afterwards. In the latter case, $\gamma_{x;\xi}(t_0)$ is called cut point and the set of all cut points of all geodesics starting from x is the cut locus $\mathcal{C}(x)$. This allows to define the inverse exponential map, also known as logarithmic map as

$$\log_x := \exp_x^{-1}: \mathcal{M} \setminus \mathcal{C}(x) \rightarrow T_x\mathcal{M}.$$

Then the Riemannian distance between $x, y \in \mathcal{M}$, for $y \notin \mathcal{C}(x)$, can be written as

$$\text{dist}(x, y) = \langle \log_x(y), \log_x(y) \rangle_x^{\frac{1}{2}} = \|\log_x(y)\|_x. \quad (4.1)$$

Let $F: \mathcal{M} \rightarrow \mathcal{N}$ be a smooth mapping between manifolds and $\xi \in T_x\mathcal{M}$. The mapping $DF(x)[\xi]$ from the set of smooth functions on a neighborhood of x to \mathbb{R} given by

$$(DF(x)[\xi])f := \xi(f \circ F)$$

is a tangent vector in $T_{F(x)}\mathcal{N}$ and the linear mapping

$$DF(x): T_x\mathcal{M} \rightarrow T_{F(x)}\mathcal{N}, \quad \xi \mapsto DF(x)[\xi]$$

the differential of F at $x \in \mathcal{M}$. Let $F: \mathcal{M}_1 \rightarrow \mathcal{M}_2$ and $G: \mathcal{M}_2 \rightarrow \mathcal{M}_3$ be two smooth mappings. Then the differential of their concatenation $G \circ F$ applied to $\xi \in T_x\mathcal{M}_1$ is given by the *chain rule*

$$D(G \circ F)(x)[\xi] = DG(F(x)) [DF(x)[\xi]].$$

For a function $f: \mathcal{M} \rightarrow \mathbb{R}$ the Riemannian gradient $\text{grad}_{\mathcal{M}}$ is defined by

$$\langle \text{grad}_{\mathcal{M}} f(x), \xi \rangle_x := Df(x)[\xi], \text{ for all } \xi \in T_x\mathcal{M}.$$

A mapping $\mathcal{R}_y: \mathcal{M} \rightarrow \mathcal{M}$ on a Riemannian manifold \mathcal{M} is called *geodesic reflection* at $x \in \mathcal{M}$ if

$$\mathcal{R}_x(x) = x \quad \text{and} \quad D(\mathcal{R}_x)(x) = -I.$$

A connected Riemannian manifold \mathcal{M} is (globally) symmetric if the geodesic reflection at any point $x \in \mathcal{M}$ is an isometry of \mathcal{M} . All manifolds considered in this paper are symmetric ones.

Let $\mathcal{X}(\mathcal{M})$ be the set of smooth vector fields on \mathcal{M} . Given a curve $\gamma: [0, 1] \rightarrow \mathcal{M}$, we denote by $\mathcal{X}(\gamma)$ the set of smooth vector fields along γ , i.e., $X \in \mathcal{X}(\gamma)$ is a smooth mapping $X: [0, 1] \rightarrow T\mathcal{M}$ with $X(t) \in T_{\gamma(t)}\mathcal{M}$. A vector field $X \in \mathcal{X}(\gamma)$ is called parallel to $\gamma: [0, 1] \rightarrow \mathcal{M}$ if the covariate derivative along γ fulfills $\frac{D}{dt}X = 0$

for all $t \in [0, 1]$. We define the *parallel transport* of a tangent vector $\xi \in T_x\mathcal{M}$ to $T_y\mathcal{M}$ by

$$P_{x \rightarrow y}\xi := X(1),$$

where $X \in \mathcal{X}(\gamma_{x,y})$ is the vector field parallel to a minimizing geodesic $\gamma_{x,y}$ with $X(0) = \xi$. There exist analytical expressions of the parallel transport only for few manifolds as spheres or positive definite matrices. However, the parallel transport can be locally approximated, e.g., by Schild's ladder [29, 44] or by the pole ladder [48]. In this paper, we focus on the pole ladder since the approximation is *exact* in symmetric Riemannian manifolds [51]. Given $x, y \in \mathcal{M}$, the pole ladder transports $\xi \in T_x\mathcal{M}$ to $\zeta \in T_y\mathcal{M}$ in four steps, cf. Fig. 4.1 left:

1. take the mid point between x and y , $c := \gamma(x, y; \frac{1}{2})$;
2. map ξ onto the manifold by the exponential map, $e := \exp_x(\xi)$;
3. evaluate the geodesic between e and c at 2, i.e. $p := \gamma(e, c; 2)$;
4. lift the end point to the tangent space of y by the logarithmic map and multiply with -1 to get $\zeta = P_{x \rightarrow y}^P(\xi) := -\log_y(p)$.

In summary, the transported vector is given by

$$P_{x \rightarrow y}^P(\xi) := -\log_y\left(\gamma\left(\exp_x(\xi), \gamma(x, y; \frac{1}{2}); 2\right)\right) \in T_y\mathcal{M}. \quad (4.2)$$

For comparison, Schild's ladder transports as follows, cf. Fig. 4.1 right:

1. map v to the manifold by the exponential map, $e := \exp_x(\xi)$;
2. take the mid point between y and e , $c := \gamma(y, e; \frac{1}{2})$;
3. evaluate the geodesic between x and c at 2, $p := \gamma(x, c; 2)$;
4. lift the point p to the tangent space of y with the logarithmic map, $w := \log_y(p)$.

The transported vector is given by

$$P_{x \rightarrow y}^S(\xi) := \log_y\left(\gamma\left(x, \gamma(y, \exp_x(\xi); \frac{1}{2}); 2\right)\right) \in T_y\mathcal{M}.$$

In our minimization algorithms, we will need the Riemannian gradient of special functions, in particular of those appearing in the pole ladder (4). This gradient can be computed for symmetric Riemannian manifolds using the theory of Jacobi fields. The following lemma collects the final results which can be partially found in [6, 20, 28]. For the complete proof we refer to [52].

Lemma 4.1 *Let \mathcal{M} be a symmetric Riemannian manifold and F one of the functions i) - v) listed below*

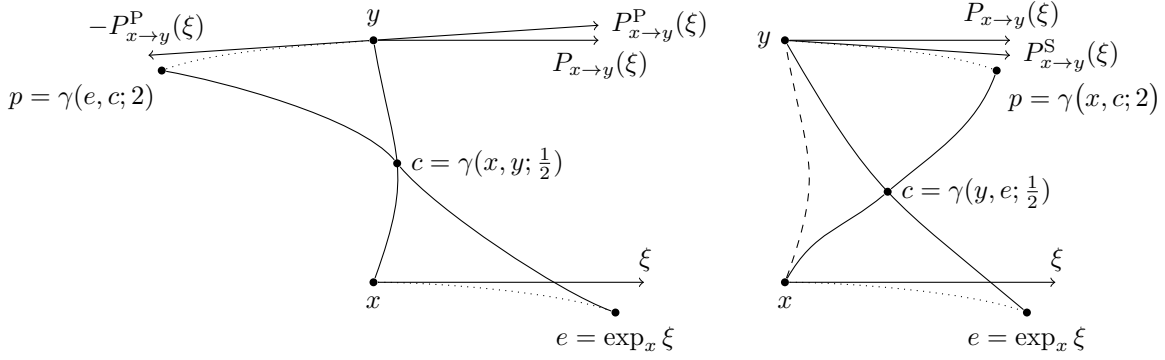


Fig. 4.1 Illustration of pole ladder (left) and Schild's ladder (right) for the approximation of $P_{x \rightarrow y} \xi$.

together with the coefficient maps $\alpha : \mathbb{R} \rightarrow \mathbb{R}$ and parameters T . Then the differential $DF(x)$ at $x \in \mathcal{M}$ is given for all $\xi \in T_x \mathcal{M}$ by

$$DF(x)[\xi] = \sum_{k=1}^d \langle \xi, \Xi_k(0) \rangle_x \alpha(\kappa_k) \Xi_k(T), \quad (4.3)$$

where $\{\Xi_k\}_{k=1}^d$ denotes a parallel transported orthogonal frame along the geodesic γ with $\gamma(0) = x$ and $\gamma(1) = y$ depending on F . Further, the frame diagonalizes the Riemannian curvature tensor $R(\cdot, \dot{\gamma})\dot{\gamma}$ with respective eigenvalues κ_k , $k = 1, \dots, d$. The functions F and α are given as follows:

i) For $F := \exp_x(u)$, we have $T = 1$, $y := \exp_x u$ and

$$\alpha(\kappa) := \begin{cases} \cosh(\sqrt{-\kappa}) & \kappa < 0, \\ 1 & \kappa = 0, \\ \cos(\sqrt{\kappa}) & \kappa > 0. \end{cases}$$

ii) For $F := \log_y(y)$, we have $T = 0$ and

$$\alpha(\kappa) := \begin{cases} -\sqrt{-\kappa} \frac{\cosh(\sqrt{-\kappa})}{\sinh(\sqrt{-\kappa})} & \kappa < 0, \\ -1 & \kappa = 0, \\ -\sqrt{\kappa} \frac{\cos(\sqrt{\kappa})}{\sin(\sqrt{\kappa})} & \kappa > 0. \end{cases}$$

iii) For $F := \log_y(\cdot)$, we have $T = 1$ and

$$\alpha(\kappa) := \begin{cases} \frac{\sqrt{-\kappa}}{\sinh(\sqrt{-\kappa})} & \kappa < 0, \\ 1 & \kappa = 0, \\ \frac{\sqrt{\kappa}}{\sin(\sqrt{\kappa})} & \kappa > 0. \end{cases}$$

iv) For $F := \gamma_{\cdot, y}(\tau)$, we have $T = \tau$ and

$$\alpha(\kappa) := \begin{cases} \frac{\sinh(\sqrt{-\kappa}(1-\tau))}{\sinh(\sqrt{-\kappa})} & \kappa < 0, \\ 1 - \tau & \kappa = 0, \\ \frac{\sin(\sqrt{\kappa}(1-\tau))}{\sin(\sqrt{\kappa})} & \kappa > 0. \end{cases}$$

v) For $F := \gamma_{y, \cdot}(\tau)$, we have $T = 1 - \tau$ and

$$\alpha(\kappa) := \begin{cases} \frac{\sinh(\sqrt{-\kappa}\tau)}{\sinh(\sqrt{-\kappa})} & \kappa < 0, \\ \tau & \kappa = 0, \\ \frac{\sin(\sqrt{\kappa}\tau)}{\sin(\sqrt{\kappa})} & \kappa > 0. \end{cases}$$

vi) Finally, we obtain for $F := \exp_x(\cdot)$ with

$$\alpha(\kappa) = \begin{cases} \frac{\sinh(\sqrt{-\kappa})}{\sqrt{-\kappa}} & \kappa < 0, \\ 1 & \kappa = 0, \\ \frac{\sin(\sqrt{\kappa})}{\sqrt{\kappa}} & \kappa > 0, \end{cases}$$

and $T = 1$ that the differential $DF(u)$ of F at $u \in T_x \mathcal{M}$ is given by (4.1), where we have to replace $x \in \mathcal{M}$ by $u \in T_x \mathcal{M}$ and to set $y := \exp_x u$.

The adjoint operator $(DF)^*(x) : T_{F(x)} \mathcal{M} \rightarrow T_x \mathcal{M}$ of (4.1) is given by

$$(DF)^*(x)[w] = \sum_{k=1}^d \langle w, \Xi_k \rangle_{F(x)} \alpha_k \xi_k, \quad w \in T_{F(x)} \mathcal{M}.$$

5 Intrinsic Models for Manifold-Valued Images

In this section, we develop intrinsic variational models to process manifold-valued images $u : \mathcal{G} \rightarrow \mathcal{M}$. Instead of the data term (2) we use

$$\mathcal{E}_{\text{data}}^{\text{int}}(u; f) = \frac{1}{2} \text{dist}^2(f, u). \quad (5.1)$$

5.1 First Order Differences

We define forward differences in x -direction by

$$(D_x^{\text{int}} u)_i := \begin{cases} \log_{u_i} u_{i+(1,0)} & \text{if } i + (1,0) \in \Gamma, \\ 0 & \text{otherwise,} \end{cases}$$

and analogously in y -direction. Then we define

$$D^{\text{int}} := \begin{pmatrix} D_x^{\text{int}} \\ \nabla_y^{\text{int}} \end{pmatrix}$$

as discrete gradient. As counterpart of (2) we introduce for $\xi = (\xi_i)_{i \in \Gamma}$ with $\xi_i \in (T_{u_i} \mathcal{M})^s$ the expression

$$\|\xi\|_{2,1,u} := \sum_{i \in \Gamma} (\|\xi_{i,1}\|_{u_i}^2 + \dots + \|\xi_{i,s}\|_{u_i}^2)^{\frac{1}{2}}.$$

Having (4) in mind, the TV regularizer for manifold-valued images becomes

$$\begin{aligned} \text{TV}^{\text{int}}(u) &:= \|\nabla^{\text{int}} u\|_{2,1,u} \\ &= \sum_{i \in \Gamma} \left(\sum_{j \in \mathcal{N}(i)} \text{dist}^2(u_i, u_j) \right)^{\frac{1}{2}}. \end{aligned} \quad (5.2)$$

The model $\mathcal{E}_{\text{data}}^{\text{int}}(u; f) + \alpha \text{TV}^{\text{int}}(u)$ was already considered in [46, 67]. Recently, several attempts have been made to translate concepts from convex analysis to the manifold-valued setting and it turns out that a rich theory of convex functions can be built in Hadamard manifolds, for an overview see, e.g., [5]. Then the functional is convex so that various algorithms as, e.g., the cyclic proximal point algorithm can be proved to converge, see [67].

5.2 Second Order Differences via Midpoints of Geodesics

To incorporate second order differences into the functional is not straightforward since there is no general definition of second order differences for manifold-valued data. We emphasize that we do not speak about Hessians of real-valued functions living on a manifold. In our case, the differences are taken with respect to Γ . If the manifold is in particular a Lie group, additions can be replaced by group operations which we will consider in the next section. In this section, we adopt the definition of the absolute value of second order differences from [6]. Observing that in the Euclidean case the absolute second order difference of $x_1, x_2, x_3 \in \mathbb{R}^d$ can be rewritten as $|x_1 - 2x_2 + x_3| = 2|\frac{1}{2}(x_1 + x_3) - x_2|$, we define a counterpart for $x_1, x_2, x_3 \in \mathcal{M}$ as

$$d_2(x_1, x_2, x_3) := \min_{c \in \mathcal{C}_{x_1, x_3}} \text{dist}(c, x_2),$$

where \mathcal{C}_{x_1, x_3} is the set of mid points $\gamma_{x_1, x_3}(\frac{1}{2})$ of all geodesics joining x_1 and x_3 . Similarly, second order mixed differences were defined for $x_i \in \mathcal{M}, i = 1, \dots, 4$, in [17]:

$$d_{1,1}(x_1, x_2, x_3, x_4) := \min_{c \in \mathcal{C}_{x_1, x_3}, \tilde{c} \in \mathcal{C}_{x_2, x_4}} \text{dist}(c, \tilde{c}).$$

We emphasize that in contrast to the TV functional TV^{int} the second order absolute difference d_2 is not convex in $x_i, i = 1, 3$ on Hadamard manifolds. However, using this definition we can introduce the absolute value of the second order difference in x -direction

$$(d_{xx}^{\text{int}} u)_i := \begin{cases} d_2(u_{i+(1,0)}, u_i, u_{i-(1,0)}) & \text{if } i \pm (1,0) \in \Gamma, \\ 0 & \text{otherwise,} \end{cases}$$

and similarly in y -direction. Note that $d_{xx}^{\text{int}}(u)_i$ is the counterpart of the *absolute value* of the Euclidean difference $\frac{1}{2}|(D_{xx}u)_i|$. The absolute value of the mixed derivative $\frac{1}{2}|(D_{xy}u)_i|$ is replaced in the manifold-valued setting by

$$(d_{xy}^{\text{int}} u)_i := \begin{cases} d_{1,1}(u_i, u_{i+(0,-1)}, u_{i+(1,0)}, u_{i+(1,-1)}) & \text{if } i \pm (0,1) \wedge i \pm (1,0) \in \Gamma, \\ 0 & \text{otherwise,} \end{cases}$$

and similarly for d_{yx}^{int} . Then we define the following counterpart of TV_2 :

$$\begin{aligned} \text{TV}_2^{\text{int}}(u) &:= \sum_{i \in \Gamma} \left((d_{xx}^{\text{int}} u)_i^2 + (d_{yy}^{\text{int}} u)_i^2 \right. \\ &\quad \left. + (d_{xy}^{\text{int}} u)_i^2 + (d_{yx}^{\text{int}} u)_i^2 \right)^{\frac{1}{2}}. \end{aligned} \quad (5.3)$$

In [6], anisotropic versions of TV^{int} and TV_2^{int} were used to set up an additive prior within a denoising model. Here we focus on the isotropic prior given by

Additive Coupling

$$\text{TV}_{1 \wedge 2}^{\text{int}}(u) := \beta \text{TV}^{\text{int}}(u) + (1 - \beta) \text{TV}_2^{\text{int}}(u).$$

Concerning our IC model we realize that in the Euclidean setting the IC of two one-homogeneous functions F_1, F_2 as for example TV and TV_2 , can be rewritten as

$$F_1 \square F_2(u) = \frac{1}{2} \inf_{u = \frac{1}{2}(v+w)} \{F_1(v) + F_2(w)\}.$$

Now we may consider the “midpoint infimal convolution” of $F_i: \mathcal{M} \rightarrow \mathbb{R}, i = 1, 2$,

$$F_1 \square_m F_2(u) := \inf_{u \in \mathcal{C}_{v,w}} \{F_1(v) + F_2(w)\},$$

in the following “Midpoint” IC prior:

Infimal Convolution (Midpoint Approach)

$$\text{IC}^{\text{int}}(u) := \inf_{u \in \mathcal{C}_{v,w}} \{\beta \text{TV}^{\text{int}}(v) \square_m (1 - \beta) \text{TV}_2^{\text{int}}(w)\}.$$

We are interested in the

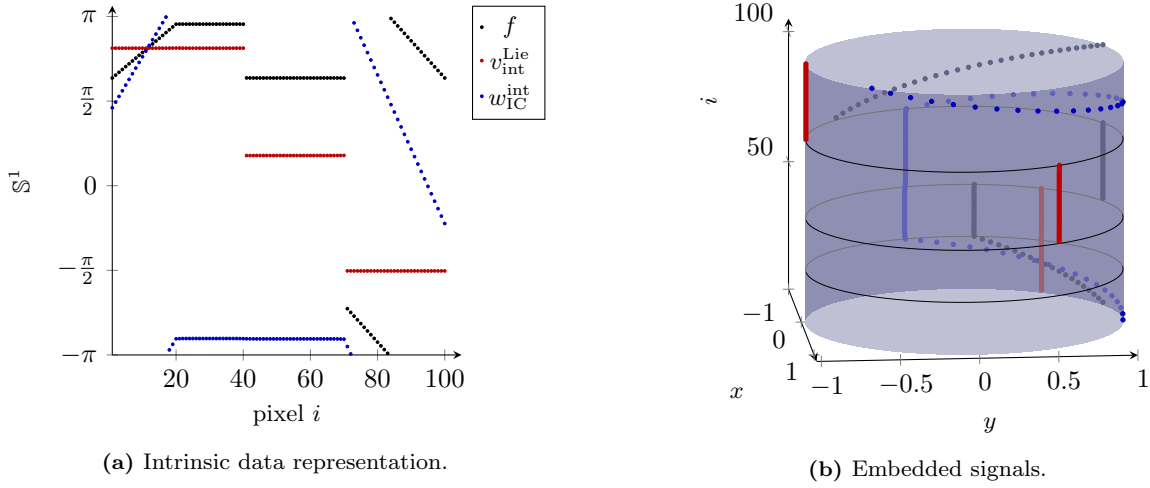


Fig. 5.1 Midpoint IC model: Decomposition of f from Fig. 3.1. (a) Original piecewise geodesic signal f (black), its the piecewise constant part $v_{\text{IC}}^{\text{Lie}}$ (red) and piecewise geodesic part $w_{\text{IC}}^{\text{int}}$ (blue) parameterized by their angles in $[-\pi, \pi)$. (b) Same signals in the embedding space \mathbb{R}^2 .

IC Decomposition (Midpoint Approach: $u = \gamma_{v,w}(\frac{1}{2})$)

$$E_{\text{IC}}^{\text{int}}(v, w) := \frac{1}{2} \sum_{i \in \Gamma} \text{dist}^2(\gamma_{v_i, w_i}(\frac{1}{2}), f_i) + \alpha(\beta \text{TV}^{\text{int}}(v) + (1 - \beta) \text{TV}_2^{\text{int}}(w)) \quad (5.4)$$

Here, $\gamma_{v_i, w_i}(\frac{1}{2})$ addresses the midpoint of the geodesic having smallest distance from f_i , for all $i \in \Gamma$, and we finally set $u := \gamma_{v,w}(\frac{1}{2})$.

Example 5.1 We consider the signal f from Fig. 3.1. Its Midpoint IC decomposition with parameters $\alpha = 0.005$, $\beta = \frac{2}{5}$ into a piecewise constant part $v_{\text{IC}}^{\text{Lie}}$ and a piecewise geodesic part $w_{\text{IC}}^{\text{int}}$ is shown in Fig. 5.1. In contrast to the extrinsic model, both parts have values in the manifold now and can be also visualized in the left plot.

5.3 Intrinsic TGV Model

TGV does not require the definition of second order differences. The first summand in the Euclidean TGV model (2) can be replaced for $\xi = (\xi_i)_{i \in \Gamma}$ with $\xi_i \in (T_{u_i} \mathcal{M})^2$ by

$$\|\nabla^{\text{int}} u - \xi\|_{2,1,u}.$$

The treatment of the backward differences $\tilde{\nabla}_S \xi$ in the second TGV summand requires to “subtract” tangent vector from different tangent spaces. For this purpose, we apply the parallel transport between the tangent

spaces. We realize the parallel transport by the pole ladder (4) which is exact in symmetric Riemannian manifolds. Then the backward difference of a vector field $\xi \in T_u \mathcal{M}^N$, i.e. $\xi_i \in T_{u_i} \mathcal{M}^N$, in x -direction reads as

$$(\tilde{D}_x^{\text{int}} \xi)_i := \begin{cases} \xi_i - P_{u_{i-(1,0)} \rightarrow u_i}^P(\xi_{i-(1,0)}) & \text{if } i \pm (1, 0) \in \Gamma, \\ 0 & \text{otherwise,} \end{cases}$$

similarly in y -direction. Application of backward differences to a vector field $\xi \in (T_u \mathcal{M}^N)^s$ is meant componentwise. In our minimization algorithms we will need the differential of the backward differences. Note that the pole ladder consists only of the concatenation of geodesics, exponential and logarithmic maps whose differentials are given in Lemma 4.1. For the differentials of the direct parallel transport in \mathbb{S}^d and $\mathcal{P}(r)$ we refer to [20]. We set

$$\tilde{\nabla}^{\text{int}} := \begin{pmatrix} \tilde{D}_x^{\text{int}} & 0 \\ \tilde{D}_y^{\text{int}} & 0 \\ 0 & \tilde{D}_x^{\text{int}} \\ 0 & \tilde{D}_y^{\text{int}} \end{pmatrix}.$$

For simplicity of computations, we use $\tilde{\nabla}^{\text{int}}$ instead of the counterpart of $\tilde{\nabla}_S$ to define a (pole ladder) TGV model by

Total Generalized Variation

$$\text{TGV}^{\text{int}}(u) := \inf_{\xi} \left\{ \beta \|\nabla^{\text{int}} u - \xi\|_{2,1,u} + (1 - \beta) \|\tilde{\nabla}^{\text{int}} \xi\|_{2,1,u} \right\}.$$

Again we are interested in the

TGV Decomposition ($\nabla^{\text{int}}u = \tilde{\xi} + \xi$)

$$E_{\text{TGV}}^{\text{int}}(u, \xi) := \frac{1}{2} \mathbf{dist}^2(u, f) + \alpha \left(\beta \|\nabla^{\text{int}}u - \xi\|_{2,1,u} + (1 - \beta) \|\tilde{\nabla}^{\text{int}}\xi\|_{2,1,u} \right). \quad (5.5)$$

Example 5.2 We apply the pole ladder TGV model (5.3) with parameters $\alpha = 0.0101$, $\beta = \frac{100}{101}$ to the signal f from Fig. 3.1. Since we have for $x \in \mathbb{S}^1$ that $T_x\mathbb{S}^1 := \{\nu \mathbf{x}^\perp : \nu u \in \mathbb{R}\}$, with the embedding $\mathbf{x} \in \mathbb{R}^2$ of x , the tangent vectors $\xi_i \in T_{u_i}$, $i = 1, \dots, 100$, can be represented by $\nu_i \in [-\pi, \pi)$, where $\xi_i = \nu_i \mathbf{u}_i^\perp$. The result is shown in Fig. 5.2 left. The signal $\nu_{\text{TGV}}^{\text{P}} := (\nu_i)_{i=1}^{100}$ approximates the finite differences of f taking its phase-valued structure into account.

Remark 5.1 (Comparison to [20]) In the parallel work [20], the authors introduced an axiomatic discrete TGV approach for manifold-valued images. In the one-dimensional setting, they proposed the prior

$$\text{TGV}^{\text{BHSW}}(u, v) := \min_v \left\{ \sum_{i \in \Gamma} \beta \mathbf{dist}(u_{i+1}, v_i) + (1 - \beta) \mathbf{dist}\left(v_i, \gamma\left(u_{i-1}, \gamma\left(u_i, v_{i-1}; \frac{1}{2}\right); 2\right)\right) \right\}.$$

In contrast to our prior, TGV^{BHSW} is directly defined on the manifold \mathcal{M} and not on $T\mathcal{M}$. Setting $v_i := \exp_{u_i} \xi_i$ we can relate the distances in TGV^{BHSW} to those in our TGV^{int} prior by

$$\begin{aligned} \mathbf{dist}(u_{i+1}, v_i) &= \mathbf{dist}(u_{i+1}, \exp_{u_i} \xi_i) \\ &\approx \|\log_{u_i} u_{i+1} - \xi_i\|_{u_i} = \|(\nabla^{\text{int}}u)_i - \xi_i\|_{u_i}, \end{aligned}$$

and

$$\begin{aligned} &\mathbf{dist}\left(v_i, \gamma\left(u_{i-1}, \gamma\left(u_i, v_{i-1}; \frac{1}{2}\right); 2\right)\right) \\ &= \mathbf{dist}\left(\exp_{u_i} \xi_i, \exp_{u_i} P_{u_{i-1} \rightarrow u_i}^{\text{S}} \xi_{i-1}\right) \\ &\approx \|\xi_i - P_{u_{i-1} \rightarrow u_i}^{\text{S}} \xi_{i-1}\|_{u_i} \approx \|\xi_i - P_{u_{i-1} \rightarrow u_i}^{\text{P}} \xi_{i-1}\|_{u_i} \\ &= \|\tilde{\nabla}_x \xi_i\|_{u_i}. \end{aligned}$$

In the two-dimensional setting, we prefer an isotropic models instead of an anisotropic one in [20]. For minimizing the TGV decomposition model we apply a gradient descent algorithm to a slightly smoothed version while the authors in [20] use a cyclic proximal point algorithm without any convergence guarantee.

6 Intrinsic Models for Lie Groups

Now we assume that the manifold \mathcal{M} is in addition a Lie group with group action $\circ: \mathcal{M} \times \mathcal{M} \rightarrow \mathcal{M}$ and unit element $e \in \mathcal{M}$. This means that the group action as well as the mapping $x \mapsto x^{-1}$, $x \in \mathcal{M}$ are smooth. For more information on Lie groups we refer to [33, 57]. In our numerical examples, \mathbb{S}^1 and $\text{SO}(3)$ are Lie groups.

The idea is to set up the different priors by replacing additions and subtractions in the Euclidean models by the group operation. All three priors are defined on the manifold now.

The *left* and *right translation* $\mathcal{L}_x, \mathcal{R}_x: \mathcal{M} \times \mathcal{M} \rightarrow \mathcal{M}$ with respect to $x \in \mathcal{M}$ are given by

$$\mathcal{L}_x(y) := x \circ y, \quad \mathcal{R}_x(y) := y \circ x,$$

respectively and

$$D\mathcal{L}_x(y)[\xi] = x \circ \xi, \quad D\mathcal{R}_x(y)[\xi] = \xi \circ x.$$

A metric on a Lie group is called right-invariant if for all $x, y \in \mathcal{M}$ and all $\xi, \zeta \in T_y\mathcal{M}$ it holds

$$\langle \xi, \zeta \rangle_y = \langle D\mathcal{R}_x(y)[\xi], D\mathcal{R}_x(y)[\zeta] \rangle_{y \circ x}$$

and similarly for the left-invariant metric. Therefore a right (left) invariant metric is induced by a metric on the tangent space $T_e\mathcal{M}$ which is actually the Lie algebra of \mathcal{M} . For matrix groups we will use the Frobenius inner product on $T_e\mathcal{M}$. Every compact Lie group, in particular \mathbb{S}^1 and $\text{SO}(3)$, admit a metric which is both left- and right-invariant, i.e. they have a bi-invariant metric. This is in general not the case as the example of Euclidean transformation group $\text{SE}(n)$, $n \geq 2$ shows, see [3]. In this section, we restrict our attention to manifolds \mathcal{M} having a right-invariant metric. Then we have for the distance function on \mathcal{M} ,

$$\mathbf{dist}(x, y) = \mathbf{dist}(x \circ y^{-1}, e) = \mathbf{dist}(e, y \circ x^{-1}). \quad (6.1)$$

This distance function is used in the the data term in (5). Replacing subtractions by appropriate group operations, we can define forward and backward “differences” in x -direction in the Lie group as

$$(D_x^{\text{Lie}}u)_i := \begin{cases} u_{i+(1,0)} \circ u_i^{-1} & \text{if } i + (1, 0) \in \Gamma, \\ e & \text{otherwise,} \end{cases}$$

and

$$(\tilde{D}_x^{\text{Lie}}u)_i := \begin{cases} u_i \circ u_{i-(1,0)}^{-1} & \text{if } i \pm (1, 0) \in \Gamma, \\ e & \text{otherwise.} \end{cases}$$

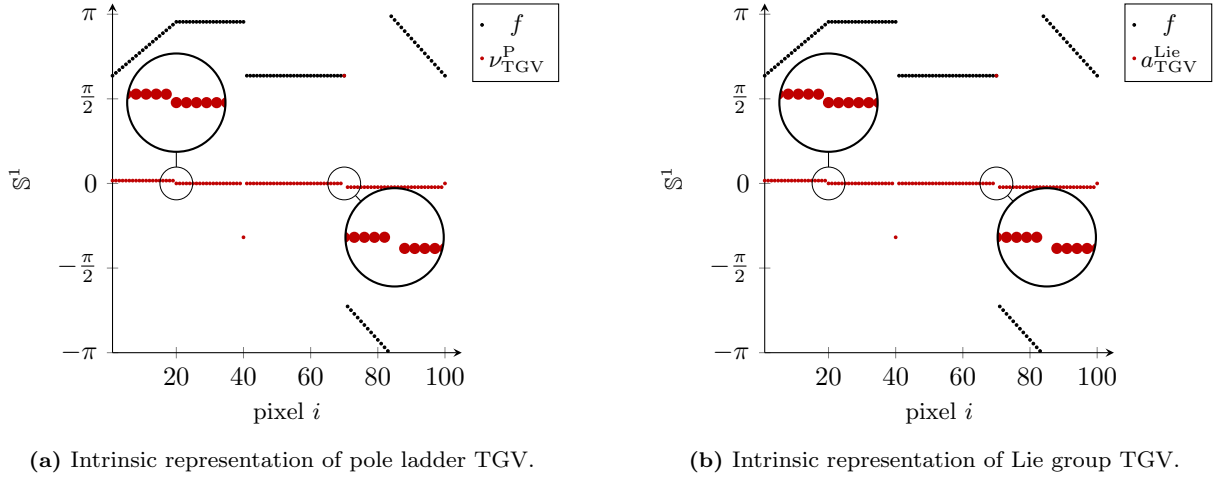


Fig. 5.2 Pole ladder TGV model (left) versus Lie group TGV model (right) applied to f from Fig. 3.1. Using $\xi_{\text{TGV}}^{\text{P}} = \nu_{\text{TGV}}^{\text{P}} \mathbf{u}^\perp$, see Example 5.2, the signal $\nu_{\text{TGV}}^{\text{P}}$ (red) can be visualized in $[-\pi, \pi)$. Interestingly, the components of the signal $\nu_{\text{TGV}}^{\text{P}}$ and $a_{\text{TGV}}^{\text{Lie}}$ from Example 6.1 differ by 3.8×10^{-4} .

and similarly in y -direction. Then we see for the manifold-valued TV term (5.1) by (6) that

$$\begin{aligned} \text{TV}^{\text{Lie}}(u) &:= \text{TV}^{\text{int}}(u) \\ &= \sum_{i \in \Gamma} \left(\text{dist}^2((D_x^{\text{Lie}} u)_i, e) + \text{dist}^2((D_y^{\text{Lie}} u)_i, e) \right)^{\frac{1}{2}}. \end{aligned}$$

Furthermore, second order differences on Lie groups resemble the concatenation of forward and backward operations the Euclidean case, e.g.,

$$(D_{xx} u)_i = (u_{i+(1,0)} - u_i) - (u_i - u_{i-(1,0)}) \text{ by}$$

$$(D_{xx}^{\text{Lie}} u)_i := \begin{cases} u_{i+(1,0)} \circ u_i^{-1} \circ u_{i-(1,0)} \circ u_i^{-1} & \text{if } i \pm (1,0) \in \Gamma, \\ e & \text{otherwise,} \end{cases}$$

and in mixed directions

$$(D_{xy}^{\text{Lie}} u)_i := \begin{cases} u_{i+(1,0)} \circ u_i^{-1} \circ u_{i-(0,1)} \circ u_{i+(1,-1)}^{-1} & \text{if } i \pm (0,1) \wedge i + (1,0) \in \Gamma, \\ e & \text{otherwise,} \end{cases}$$

and similarly for D_{yy}^{Lie} and D_{yx}^{Lie} . Then, with

$$(d_*^{\text{Lie}} u)_i^2 := \text{dist}((D_*^{\text{Lie}} u)_i, e), \quad * \in \{xx, yy, xy, yx\},$$

we define

$$\begin{aligned} \text{TV}_2^{\text{Lie}}(u) &:= \sum_{i \in \Gamma} \left((d_{xx}^{\text{Lie}} u)_i^2 + (d_{yy}^{\text{Lie}} u)_i^2 \right. \\ &\quad \left. + (d_{xy}^{\text{Lie}} u)_i^2 + (d_{yx}^{\text{Lie}} u)_i^2 \right)^{\frac{1}{2}}. \end{aligned}$$

Now the additive and IC prior on Lie groups can be introduced as follows:

Additive Coupling

$$\text{TV}_{1 \wedge 2}^{\text{Lie}}(u) := \beta \text{TV}^{\text{Lie}}(u) + (1 - \beta) \text{TV}_2^{\text{Lie}}(u).$$

Infimal Convolution

$$\text{IC}^{\text{Lie}}(u) := \inf_{u=v \circ w} \{ \beta \text{TV}^{\text{Lie}}(v) + (1 - \beta) \text{TV}_2^{\text{Lie}}(w) \}.$$

Again, we are interested in the splitting model:

IC Decomposition ($u = v \circ w$)

$$\begin{aligned} E_{\text{IC}}^{\text{Lie}}(v, w) &:= \frac{1}{2} \text{dist}^2(f, v \circ w) \\ &\quad + \alpha (\beta \text{TV}^{\text{Lie}}(v) + (1 - \beta) \text{TV}_2^{\text{Lie}}(w)). \end{aligned} \quad (6.2)$$

Since we just apply group operations to define „differences“ the TGV prior is also defined on the Lie group by

Total Generalized Variation

$$\begin{aligned} \text{TGV}^{\text{Lie}}(u) &:= \inf_{a=(a_1, a_2)} \left\{ \beta \left(\text{dist}(D_x^{\text{Lie}} u, a_1)^2 + \text{dist}(D_y^{\text{Lie}} u, a_2)^2 \right)^{\frac{1}{2}} \right. \\ &\quad \left. + (1 - \beta) \left(\text{dist}(\tilde{D}_x^{\text{Lie}} a_1, e)^2 + \text{dist}(\tilde{D}_y^{\text{Lie}} a_2, e)^2 \right. \right. \\ &\quad \left. \left. + \text{dist}(\tilde{D}_y^{\text{Lie}} a_1, e)^2 + \text{dist}(\tilde{D}_x^{\text{Lie}} a_2, e)^2 \right)^{\frac{1}{2}} \right\}. \end{aligned} \quad (6.3)$$

Actually, we are interested in the following decomposition:

TGV Decomposition ($((D_x^{\text{Lie}} u, D_y^{\text{Lie}} u)^T = (\tilde{a}_k \circ a_k)_{k=1}^2$)

$$\begin{aligned} E_{\text{TGV}}^{\text{Lie}}(u, a) &:= \frac{1}{2} \text{dist}^2(f, u) \\ &\quad + \alpha \left(\beta \left(\text{dist}(D_x^{\text{Lie}} u, a_1)^2 + \text{dist}(D_y^{\text{Lie}} u, a_2)^2 \right)^{\frac{1}{2}} \right. \\ &\quad \left. + (1 - \beta) \left(\text{dist}(\tilde{D}_x^{\text{Lie}} a_1, e)^2 + \text{dist}(\tilde{D}_y^{\text{Lie}} a_2, e)^2 \right. \right. \\ &\quad \left. \left. + \text{dist}(\tilde{D}_y^{\text{Lie}} a_1, e)^2 + \text{dist}(\tilde{D}_x^{\text{Lie}} a_2, e)^2 \right)^{\frac{1}{2}} \right) \end{aligned} \quad (6.4)$$

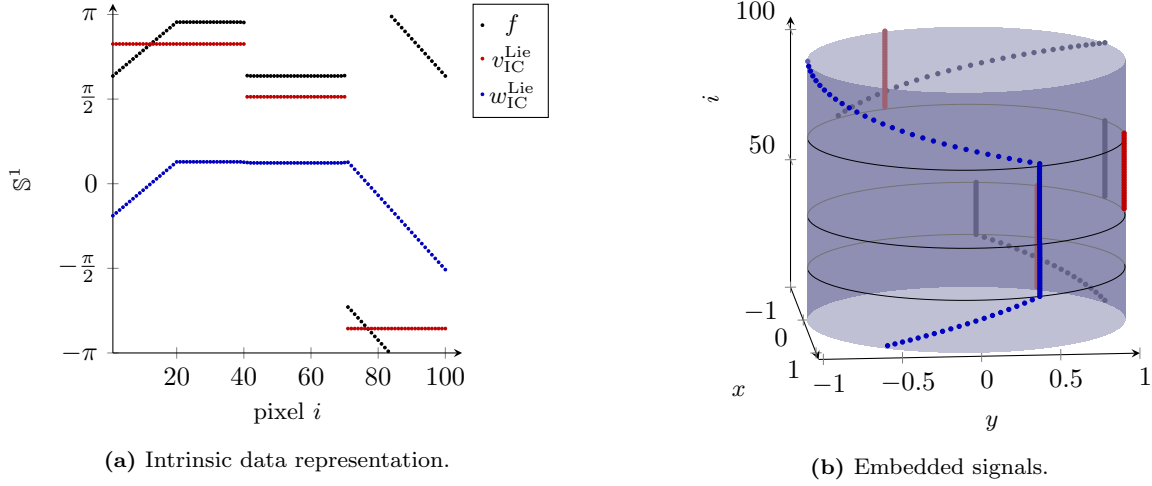


Fig. 6.1 Lie group IC model: Decomposition of f from Fig. 3.1. (a) Original piecewise geodesic signal f (black) determined by its angles in $[-\pi, \pi)$, the piecewise constant component $v_{\text{IC}}^{\text{Lie}}$ (red), and piecewise geodesic component $w_{\text{IC}}^{\text{Lie}}$ (blue). In contrast to the Midpoint IC model, the decomposed parts have other slopes and jump heights. (b) Same signals in the embedding space \mathbb{R}^2 .

Example 6.1 First, we apply the Lie group IC model (6) with parameters $\alpha = 0.001$, $\beta = \frac{2}{3}$ to the signal f in Fig. 3.1. The result is shown in Fig. 6.1. As expected, the piecewise constant part $v_{\text{IC}}^{\text{Lie}}$ contains the jumps and the second order component $w_{\text{IC}}^{\text{Lie}}$ is piecewise geodesic. Due to the construction, the main difference to the result of the Midpoint IC model is the slope of the piecewise geodesic parts and the jump height of the piecewise constant part.

Next, we apply the Lie group TGV model (6) with parameters $\alpha = 0.001$, $\beta = \frac{2}{3}$. The result is depicted in Fig. 5.2 right. Interestingly, comparing $\nu_{\text{TGV}}^{\text{P}}$ with $a_{\text{TGV}}^{\text{Lie}}$, we do not see a difference in the plot.

7 Gradient Descent for the Intrinsic Models

To compute critical points of the intrinsic models we apply gradient descent algorithms. To make the priors differentiable, we have to add a small positive value $\varepsilon^2 \ll 1$ within the square roots appearing in TV^* , TV_2^* and TGV^* , $*$ $\in \{\text{int}, \text{Lie}\}$. For the intrinsic IC models $E_{\text{IC}}^{\text{int}}$, $E_{\text{IC}}^{\text{Lie}}$ defined on $(\mathcal{M}^N)^2$ and $E_{\text{TGV}}^{\text{Lie}}$ defined on $(\mathcal{M}^N)^3$ we apply the gradient descent Algorithm 1. We use the notation

$$\mathbf{M} := (\mathcal{M}^N)^s, \quad s \in \{2, 3\}.$$

For the $E_{\text{TGV}}^{\text{int}}$ model which is defined on the manifold and the tangent bundle, we propose Algorithm 2.

Proposition 7.1 i) *For any of the functionals $E_{\text{IC}}^{\text{int}}$, $E_{\text{IC}}^{\text{Lie}}$, and $E_{\text{TGV}}^{\text{Lie}}$, every accumulation point of the sequence $(p^{(r)})_{r \in \mathbb{N}}$ generated by Algorithm 1 is a critical point.*

Algorithm 1 Gradient Descent for

$E: \mathbf{M} \rightarrow \mathbb{R}$ from $\{E_{\text{IC}}^{\text{int}}, E_{\text{IC}}^{\text{Lie}}, E_{\text{TGV}}^{\text{Lie}}\}$

Input: $p^{(0)} \in \mathbf{M}$; $c, \sigma > 0$; $\rho \in (0, 1)$

Output: $\hat{p} \in \mathbf{M}$

$r = 0$

repeat

Choose the smallest $l \in \mathbb{N}$ fulfilling the Armijo condition

$$E(p^{(r)}) - c\sigma\rho^l \|\text{grad}_{\mathbf{M}} E(p^{(r)})\|^2 \geq E(p_l^{(r)})$$

with

$$p_l^{(r)} := \exp_{p^{(r)}}(-\rho^l \sigma \text{grad}_{\mathbf{M}} E(p^{(r)}))$$

Set

$$p^{(r+1)} := \exp_{p^{(r)}}(-\rho^l \sigma \text{grad}_{\mathbf{M}} E(p^{(r)}))$$

$r \leftarrow r + 1$;

until a stopping criterion is reached;

$\hat{p} = p^{(r)}$;

ii) *For the functional $E_{\text{TGV}}^{\text{int}}$, every accumulation point of the sequence $(u^{(r)}, \xi^{(r)})_{r \in \mathbb{N}}$ generated by Algorithm 2 is a critical point.*

Proof. Part i) follows by [1, Theorem 4.3.1].

Concerning ii) we recognize that Algorithm 2 is a descent algorithm on $\mathcal{M}^N \times (T\mathcal{M}^N)^2$ [53, 59] with an Armijo step size rule. Hence the assumption follows by [1, Theorem 4.3.1]. \square

To obtain the gradients in Algorithm 1 and 2 we have to compute the gradients of all involved summands. In the rest of this section, we sketch their computation. We restrict our attention to symmetric Riemannian manifolds and Lie groups with bi-invariant metric.

Algorithm 2 Gradient Descent for $E := E_{\text{TGV}}^{\text{int}}$

Input: $u^{(0)} \in \mathcal{M}^N$; $\xi^{(0)} \in (T_{u^{(0)}}\mathcal{M}^N)^2$;
 $\sigma, c > 0$; $\rho \in (0, 1)$

Output: $\hat{u} \in \mathcal{M}^N$, $\hat{\xi} \in (T_{\hat{u}}\mathcal{M}^N)^2$

$r = 0$;

repeat

 Compute

$$b^{(r)} := -\text{grad}_{(T\mathcal{M}^N)^2, \xi}(E(u^{(r)}, \cdot))(\xi^{(r)})$$

$$v^{(r)} := -\text{grad}_{\mathcal{M}^N, u}(E(\cdot, \xi^{(r)}))(u^{(r)})$$

 Choose the smallest $l \in \mathbb{N}$ fulfilling the Armijo condition

$$E(u^{(r,l)}, \xi^{(r,l)}) \leq E(u^{(r)}, v^{(r)}) - c\sigma\rho^l (\|v^{(r)}\|_{u^{(r)}}^2 + \|b_1^{(r)}\|_{u^{(r)}}^2 + \|b_2^{(r)}\|_{u^{(r)}}^2)$$

 with

$$u^{(r,l)} := \exp_{u^{(r)}}(\sigma\rho^l v^{(r)})$$

$$\xi_1^{(r,l)} := P_{u^{(r)} \rightarrow u^{(r,l)}}(\xi_1^{(r)} + \sigma\rho^l b_1^{(r)})$$

$$\xi_2^{(r,l)} := P_{u^{(r)} \rightarrow u^{(r,l)}}(\xi_2^{(r)} + \sigma\rho^l b_2^{(r)})$$

 Set

$$u^{(r+1)} := u^{(r,l)}$$

$$\xi^{(r+1)} := \xi^{(r,l)}$$

$r \leftarrow r + 1$

until a stopping criterion is reached;

$$(\hat{u}, \hat{\xi}) := (u^{(r)}, \xi^{(r)})$$

for a detailed treatment of all involved Riemannian gradients we refer to [52].

The gradients of the data term $\mathcal{E}_{\text{data}}^{\text{int}}$ in (5) and the smoothed terms $\text{TV}^{\text{int}} = \text{TV}^{\text{Lie}}$ in (5.1) can be obtained by the chain rule and

$$\text{grad}_{\mathcal{M}} \text{dist}^2(\cdot, y)(x) = -2 \log_x y. \quad (7.1)$$

For TV_2^{int} in (5.2) we can apply the the gradient computations of d_{\star}^{int} , $\star \in \{xx, yy, xy, yx\}$, detailed in [6] together with the chain rule. The gradient of $\text{dist}^2(\gamma_{v_i, w_i}(\frac{1}{2}), f_i)$ in the data term of $E_{\text{IC}}^{\text{int}}$ in (5.2) follows by the chain rule and Lemma 4.1 iv) and v). The gradient of $\text{dist}^2(f_i, \cdot \circ w_i)$ in the data term of $E_{\text{IC}}^{\text{Lie}}$ in (6) can be obtained by

$$\begin{aligned} \text{grad}_{\mathcal{M}, v_i} \left(\text{dist}^2(f, \cdot \circ w) \right) (v_i) \\ = \text{grad}_{\mathcal{M}, v_i} \left(\text{dist}^2(f \circ w^{-1}, \cdot) \right) (v_i) \\ = -2 \log_{v_i} (f_i \circ w_i^{-1}) \end{aligned}$$

using the right invariance of the geodesic distance. Similarly, we compute the gradient with respect to w using the left invariance of the metric. To get the gradient of TV_2^{Lie} we apply the chain rule with the following lemma.

Lemma 7.1 *The gradients of $(d_{xx}^{\text{Lie}})^2$ and $(d_{xy}^{\text{Lie}})^2$ are given by*

$$\begin{aligned} \text{grad}_{\mathcal{M}, w_i} (d_{xx}^{\text{Lie}})_i^2(w) = -2(\\ D\mathcal{L}_{w_{i-(1,0)} \circ w_i^{-1}} [\log_{w_i \circ w_{i-(1,0)}^{-1} \circ w_i} w_{i+(1,0)}] \\ + D\mathcal{R}_{w_i^{-1} \circ w_{i-(1,0)}} [\log_{w_i \circ w_{i-(1,0)}^{-1} \circ w_i} w_{i+(1,0)}]) \end{aligned}$$

and

$$\begin{aligned} \text{grad}_{\mathcal{M}, w_i} (d_{xy}^{\text{Lie}})_i^2(w) \\ = -2 \log_{w_i} (w_{i-(0,1)} \circ w_{i+(1,-1)}^{-1} \circ w_{i+(1,0)}). \end{aligned}$$

The proof is given in Appendix.

The summands in the TGV prior on Lie groups (6) have a similar structure as those in the Lie group IC model. The computation is even simpler since no argument exists twice in one distance term. Therefore the gradients can be calculated by isolating the arguments of interest on one side of the distance function and then apply the chain rule with (7).

It remains to consider the gradient of the TGV^{int} prior in (5.3). Due to symmetries we may stick to the one-dimensional case. Further, we abbreviate the differentials from Lemma 4.1 by

$$\begin{aligned} E_x(u) &:= D(\exp_x \cdot)(\xi): T_x \mathcal{M} \rightarrow T_y \mathcal{M}, \quad y := \exp_x \xi, \\ \tilde{E}_u(x) &:= D(\exp(\cdot))(x): T_x \mathcal{M} \rightarrow T_y \mathcal{M}, \\ L_x(y) &:= D(\log_x \cdot)(y): T_y \mathcal{M} \rightarrow T_x \mathcal{M}, \\ \tilde{L}_y(x) &:= D(\log(\cdot))(x): T_x \mathcal{M} \rightarrow T_y \mathcal{M}, \\ G_{\cdot, y, \tau}(x) &:= D\gamma(\cdot, y; \tau)(x): T_x \mathcal{M} \rightarrow T_{\gamma_{x, y}(\tau)} \mathcal{M}, \\ G_{x, \cdot, \tau}(y) &:= D\gamma(x, \cdot; \tau)(y): T_y \mathcal{M} \rightarrow T_{\gamma_{x, y}(\tau)} \mathcal{M}. \end{aligned}$$

Then the gradients can be derived by the chain rule and the following lemma.

Lemma 7.2 *The functions*

$$\begin{aligned} F_1(u_i, u_{i+1}, \xi_i) &:= \|\log_{u_i} u_{i+1} - \xi_i\|_{u_i}^2, \\ F_2(u_i, u_{i-1}, \xi_i, \xi_{i-1}) &:= \|\xi_i - P_{u_{i-1} \rightarrow u_i}^{\text{P}}(\xi_{i-1})\|_{u_i}^2 \end{aligned}$$

have the Riemannian gradients

$$\text{grad}_{\mathcal{M}, \xi_i} F_1(u_i, u_{i+1}, \cdot)(\xi_i) = 2(\xi_i - \log_{u_i} u_{i+1}) =: -T,$$

$$\text{grad}_{\mathcal{M}, u_i} F_1(\cdot, u_{i+1}, \xi_i)(u_i) = \tilde{L}_{u_{i+1}}^*(u_i)[T]$$

$$\text{grad}_{\mathcal{M}, u_{i+1}} F_1(u_i, \cdot, \xi_i)(u_{i+1}) = L_{u_i}^*(u_{i+1})[T],$$

and

$$\begin{aligned}
& \text{grad}_{\mathcal{M}, \xi_i} F_2(u_i, u_{i-1}, \cdot, \xi_{i-1})(\xi_i) \\
& \quad = 2(\xi_i - P_{u_{i-1} \rightarrow u_i}^P(\xi_{i-1})) =: -S, \\
& \text{grad}_{\mathcal{M}, \xi_{i-1}} (F_2(u_i, u_{i-1}, \xi_i, \cdot))(\xi_{i-1}) \\
& \quad = E_{u_{i-1}}^*(\xi_{i-1}) \left[G_{\cdot, c_i, 2}^*(e_i) [L_{u_i}^*(p_i)[S]] \right], \\
& \text{grad}_{\mathcal{M}, u_i} (F_2(\cdot, u_{i-1}, \xi_i, \xi_{i-1}))(u_i) \\
& \quad = \tilde{L}_{p_i}^*(u_i)[S] \\
& \quad \quad + G_{\cdot, u_{i-1}, \frac{1}{2}}^*(u_i) \left[G_{e_i, \cdot, 2}^*(c_i) [L_{u_i}^*(p_i)[S]] \right], \\
& \text{grad}_{\mathcal{M}, u_{i-1}} (F_2(u_i, \cdot, \xi_i, \xi_{i-1}))(u_{i-1}) \\
& \quad = \tilde{E}_{\xi_{i-1}}^*(u_{i-1}) \left[G_{\cdot, c_i, 2}^*(e_i) [L_{u_i}^*(p_i)[S]] \right] \\
& \quad \quad + G_{u_i, \cdot, \frac{1}{2}}^*(u_{i-1}) \left[G_{e_i, \cdot, 2}^*(c_i) [L_{u_i}^*(p_i)[S]] \right],
\end{aligned}$$

where we set $e_i := \exp_{u_{i-1}}(\xi_{i-1})$, $c_i := \gamma(u_i, u_{i-1}; \frac{1}{2})$ and $p_i := \gamma(e_i, c_i; 2)$.

The proof is given in the appendix.

8 Numerical examples

The gradient descent algorithm and ADMM are implemented in MATLAB. The basic manifold functions, like logarithmic and exponential maps, as well as the distance function are implemented as C++ functions within the „Manifold-valued Image Restoration Toolbox“(MVIRT)¹ and imported into MATLAB using `mex`-interfaces with the GCC 4.8.4 compiler. As a quality measure we use the mean squared error (MSE) defined by

$$\epsilon := \frac{1}{|\Gamma|} \sum_{i \in \Gamma} \text{dist}^2(u_i, u_{0,i}),$$

where u_0 denotes the original image. The parameters in the artificial examples are adapted via grid search to minimize this measure ϵ . The relaxation parameter ε is chosen for each experiment based on the data. The algorithm stops if one of the following criteria is fulfilled

- the maximal change is small enough, i.e.,

$$\max_{i \in \Gamma} \{\text{dist}(p_i^{(r)}, p_i^{(r-1)})\} < \delta,$$

with $\delta = 10^{-10}$ for signals and $\delta = 10^{-8}$ for images;

- the number of iterations exceeds $c \in \mathbb{N}$, i.e., $r > c$, with $c = 10^6$ for signals and $c = 10^5$ for images.

8.1 \mathbb{S}^1 -valued data

We start with the \mathbb{S}^1 -valued image in Fig. 8.1 (a) from [14]. Adding wrapped Gaussian noise results in the corrupted image (b). In [14] the additive $\text{TV}_{1 \wedge 2}$ yields to an error of $\epsilon = 5.4 \times 10^{-3}$. Comparing this result to the pole ladder TGV ($\alpha = 1$, $\beta = 0.3$, $\varepsilon = 10^{-3}$), see (c) and Lie group TGV ($\alpha = 1$, $\beta = 0.3$, $\varepsilon = 10^{-6}$), cf. (d), we see that the TGV models yield a smaller error. These models are able to nicely reconstruct the linear parts in the ellipsoid and the edges of the boxes. Compared to the nonlocal methods [45] and [15] shown in (e) and (f), respectively, the TGV models have nearly the same error. However, looking at the paraboloid in the bottom right corner, they outperform the nonlocal methods visually.

8.2 \mathbb{S}^2 -valued data

Now we are interested in \mathbb{S}^2 valued signals, where the Lie group approach cannot be applied. First, we are interested in the decomposition of a signal. The ground truth signal in Fig. 8.2 is obtained as follows: we take three great arcs from the north pole to the equator, a quarter great arc along the equator, and from thereon further to the south pole. We scale the segments by $\frac{1}{5}$, $\frac{3}{20}$, and $\frac{1}{5}$, respectively such that we obtain jumps between the three geodesic segments. This yields a signal of length 192 shown in Fig. 8.2 (b). We apply the Midpoint IC model with $\alpha = \frac{11}{100}$, $\beta = \frac{1}{11}$. The result u approximates f and its decomposition into v and w yields signals that are nearly piecewise constant and piecewise geodesic, respectively.

Next we present a denoising result. In Fig. 8.3 we compare intrinsic additive model with the Midpoint IC and pole ladder TGV approach. The original signal consists of four segments of length 20; the first two are geodesic segments, then there is a jump to a constant segment, and the last segment is again geodesic. Fig. 8.3 (a) shows the original and the corrupted signal with Gaussian noise ($\sigma = 0.1$). The parameters for the additive model are $\alpha\beta = \frac{1}{10}$ and $\alpha(1 - \beta) = 4.6$, for the Midpoint IC $\alpha = \frac{1}{2}$, $\beta = 0.3$, $\varepsilon = 10^{-3}$ and for the pole ladder TGV model $\alpha = \frac{3}{5}$, $\beta = 0.3$ and we relax by $\varepsilon = 10^{-5}$. The results are shown in 8.3 (b) to (d). In comparison to the additive model the IC and TGV models preserve the jump better and yield a lower error. Comparing the IC and TGV model we see that the TGV model is more suited to reconstruct the geodesic parts. Hence, it yields the lowest error ϵ .

¹ <http://www.mathematik.uni-kl.de/imagepro/members/bergmann/mvirt/>

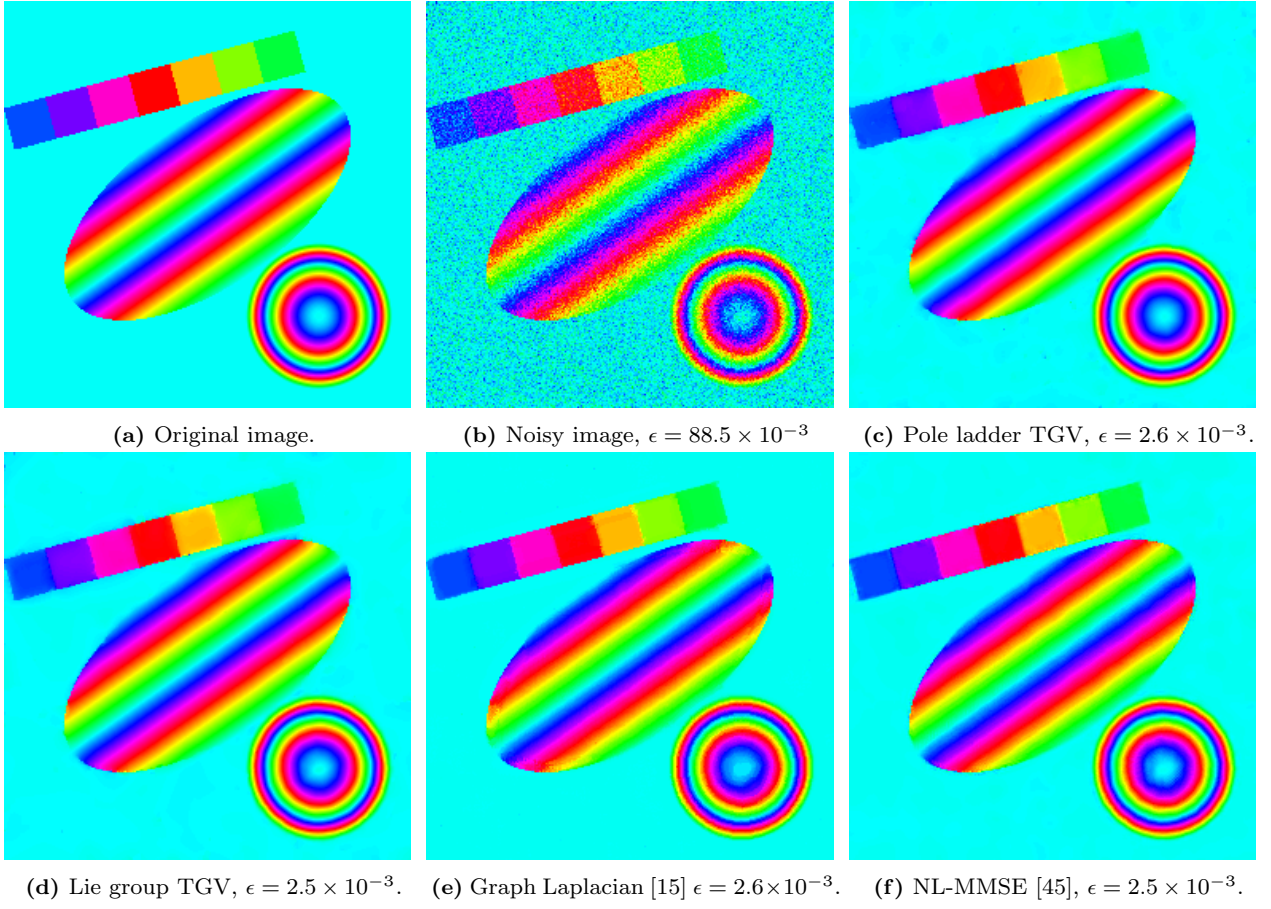


Fig. 8.1 Denoising of an artificial S^1 image with different methods.

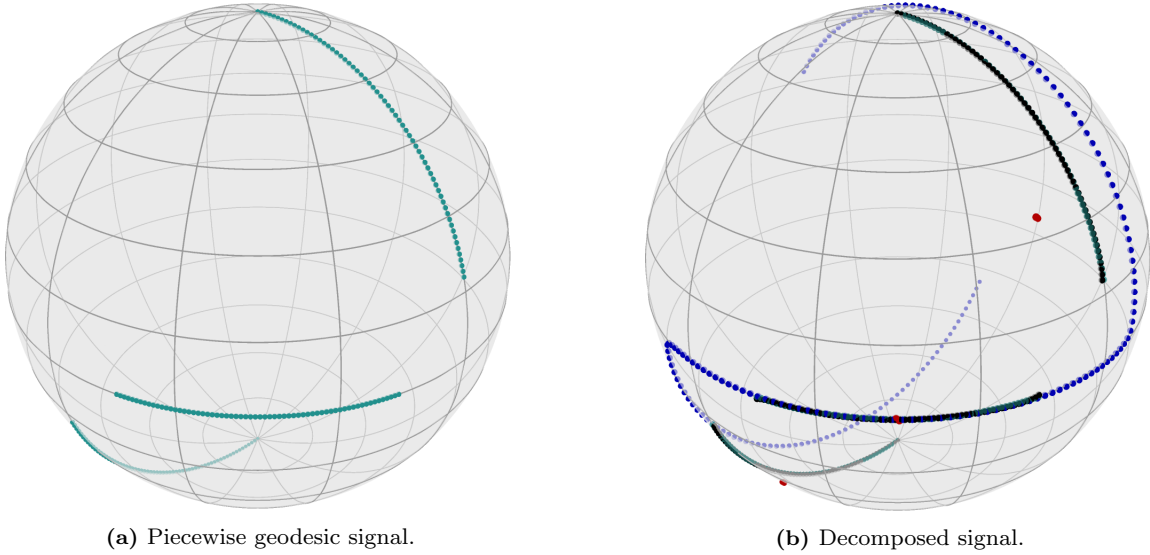


Fig. 8.2 Midpoint IC decomposition of a piecewise geodesic signal f (green), into a piecewise constant part v (red) and a continuous piecewise geodesic curve w (blue). The mid point signal $u = \gamma_{v,w}(\frac{1}{2})$ (black) nearly reconstructs f (green).

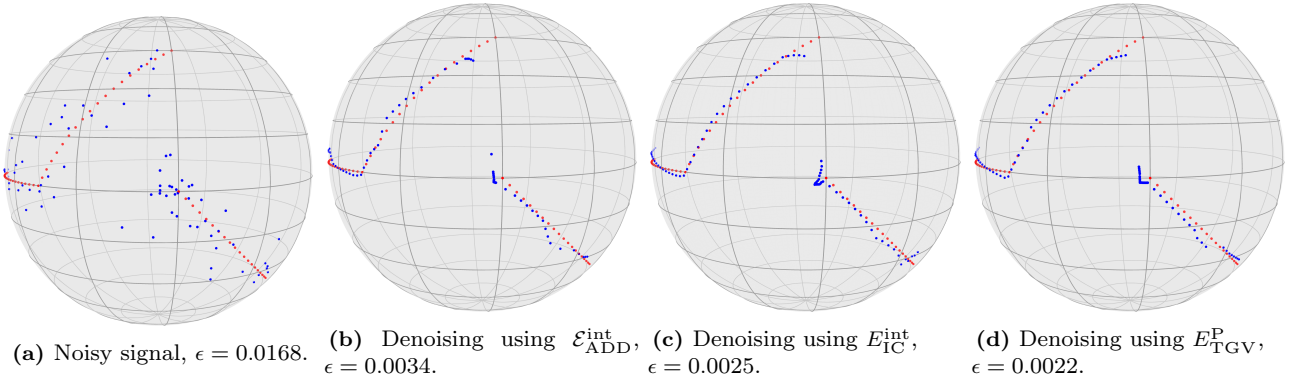


Fig. 8.3 Denoising of a S^2 -valued signal with additive and TGV priors. The original signal is plotted in red and the noisy/restored signals in blue.

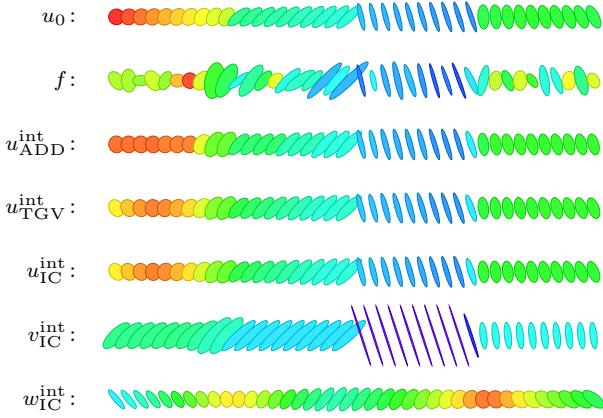


Fig. 8.4 Denoising and decomposition of a $\mathcal{P}(2)$ valued signal f . Denoising result $u_{\text{ADD}}^{\text{int}}$ by additive model with prior $\text{TV}_{1\wedge 2}^{\text{int}}$, $\epsilon = 0.0316$, with the TGV model, $\epsilon = 0.0259$, and $u_{\text{IC}}^{\text{int}}$ by Midpoint IC model, $\epsilon = 0.0269$. Decomposition by Midpoint IC model gives $v_{\text{IC}}^{\text{int}}$ and geodesic part $w_{\text{IC}}^{\text{int}}$ with geodesic midpoint $u_{\text{IC}}^{\text{int}}$.

8.3 SPD-valued data

In this subsection, we consider the decomposition and denoising of SPD-valued data. Fig. 8.4 shows a signal u_0 with values in $\mathcal{P}(2)$ which is the midpoint of a signal with four constant parts and one with two geodesic parts. The signal f is its noisy version with Gaussian noise. We apply the intrinsic additive model ($\alpha = 0.46, \beta = 1$), the intrinsic TGV model ($\alpha = 2.5, \beta = 0.2$), and the Midpoint IC model ($\alpha = 4.5, \beta = \frac{1}{9}$) to f . Here we use $\varepsilon = 10^{-3}$ as relaxation. With respect to both the MSE and visually the TGV and Midpoint IC model outperform the additive one. In particular, the smooth parts are better reconstructed. The results from the sophisticated intrinsic priors are very similar and visually not distinguishable. The compo-

nents v and w from the IC model give a decomposition of u_0 into a piecewise constant and geodesic component.

Fig. 8.5 (a) shows an artificial $\mathcal{P}(3)$ -valued image which is corrupted by Gaussian noise ($\sigma = 0.1$) resulting in (b). The result of the extrinsic TGV model $u_{\text{TGV}}^{\text{ext}}$ ($\alpha = 12, \beta = 0.9$) is shown in (d) and the extrinsic IC model $u_{\text{IC}}^{\text{ext}}$ ($\alpha = 4, \beta = 0.4$) in (c). As the geodesics in $\mathcal{P}(3)$ are not linear in the embedding it is advantageous to use intrinsic models to denoise the image. The pole ladder TGV model ($\alpha = 0.7, \beta = 0.3, \varepsilon = 10^{-4}$) yields the result in (e), which has a lower error as the extrinsic methods. Denoising with the Midpoint IC model ($\alpha = \frac{1}{10}, \beta = \frac{1}{2}, \varepsilon = 10^{-5}$) leads to the denoised image $u_{\text{IC}}^{\text{int}}$ (f). The corresponding IC components depicted in (g) and (h) show nicely the piecewise constant part $v_{\text{IC}}^{\text{int}}$ containing the jump and the geodesic part $w_{\text{IC}}^{\text{int}}$.

8.4 SO(3)-valued data

EBSD is often given as images having values $[f_i]$ in the quotient $\text{SO}(3)/S$ of the Lie group $\text{SO}(3)$, where $S \subset \text{SO}(3)/S$ denotes the symmetry group of the crystal structure in point i . EBSD images usually consist of regions with similar orientations called grains. Fig. 8.6 displays a typical EBSD image of a magnesium specimen from the software package MTEX [7] which is also used for the color visualizing the data. For certain macroscopic properties the pattern of orientations within single grains is important, see e.g., [8, 64].

Fig. 8.7 displays the single grain at the lower right corner of Fig. 8.6. Since the rotations vary little within a single grain, we treat the data as $\text{SO}(3)$ -valued. Within this single grain there occurs a so-called subgrain boundary which should be preserved during denoising. We compare results of the different IC models. Note that we apply a different colorization for the component w

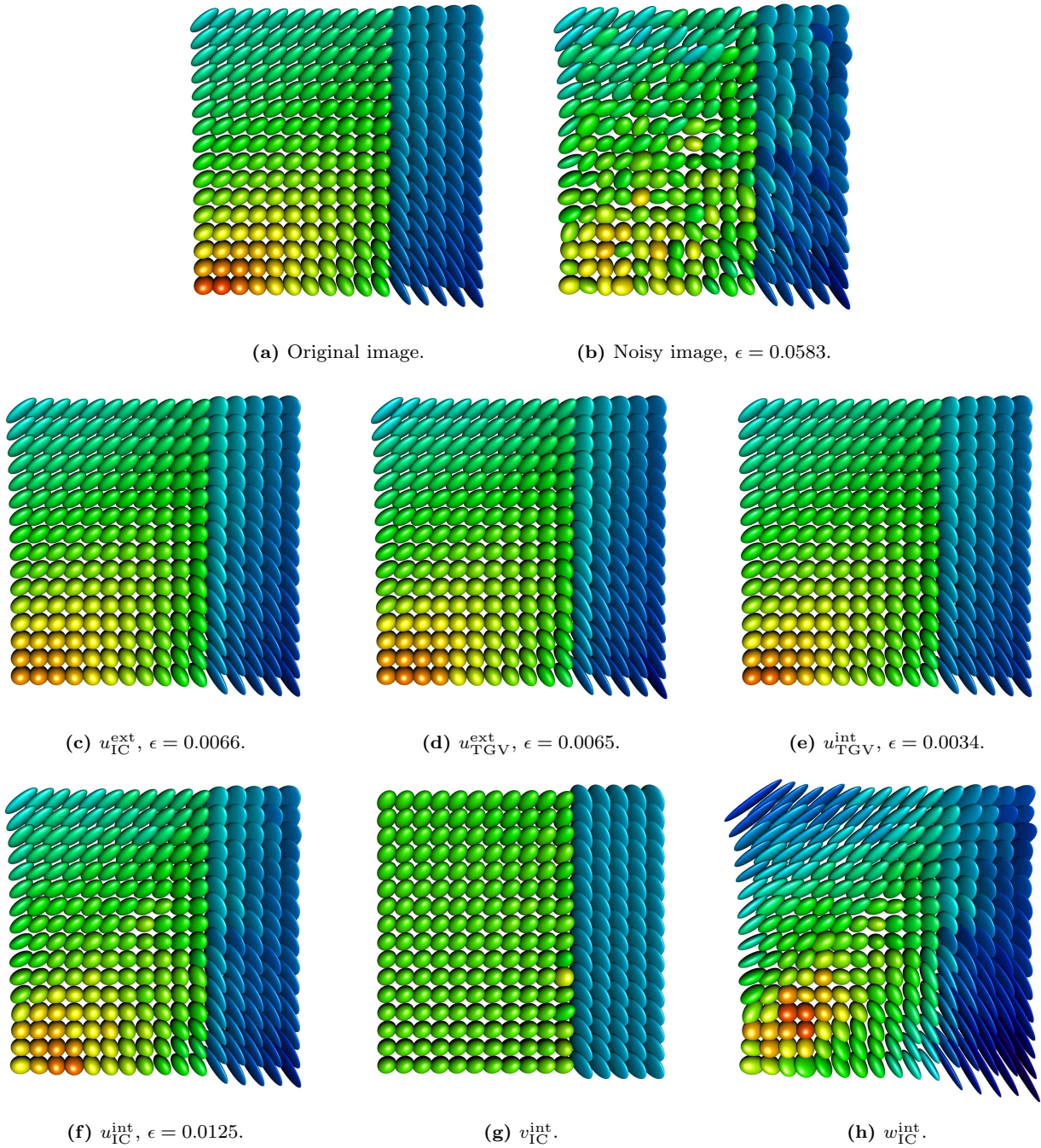


Fig. 8.5 Denoising of an artificial $\mathcal{P}(3)$ -valued image with extrinsic and Midpoint IC model.

by placing the center of the colormap at the Karcher mean of the samples and using the same stretching factor for all w . The denoising result of the extrinsic IC model ($\alpha = 0.06$, $\beta = \frac{1}{3}$) are similar to those if the Midpoint IC model $\alpha = \frac{1}{20}$, $\beta = \frac{1}{3}$ and the Lie group IC model ($\alpha = \frac{1}{20}$, $\beta = \frac{1}{3}$). The component v penalized with the TV term has a piecewise constant structure, cf. Fig. 8.7(d) and (g), while the w part is smooth, see Fig. 8.7(e) and (h). Even though, we used the same

set of parameters for both approaches, we observe some differences. The v_{IC}^{int} -component of the mid point model has a larger jump, which is expected, as the jump should match twice the jump in the original signal. The w_{IC}^{int} -component on the other hand has less movement as w_{IC}^{Lie} of the Lie group model. The TV_2^{int} regularizes stronger as the Lie group counterpart. This effect is also visible in the reconstructed images, i.e., u_{IC}^{Lie} is more constant, as the other two results.

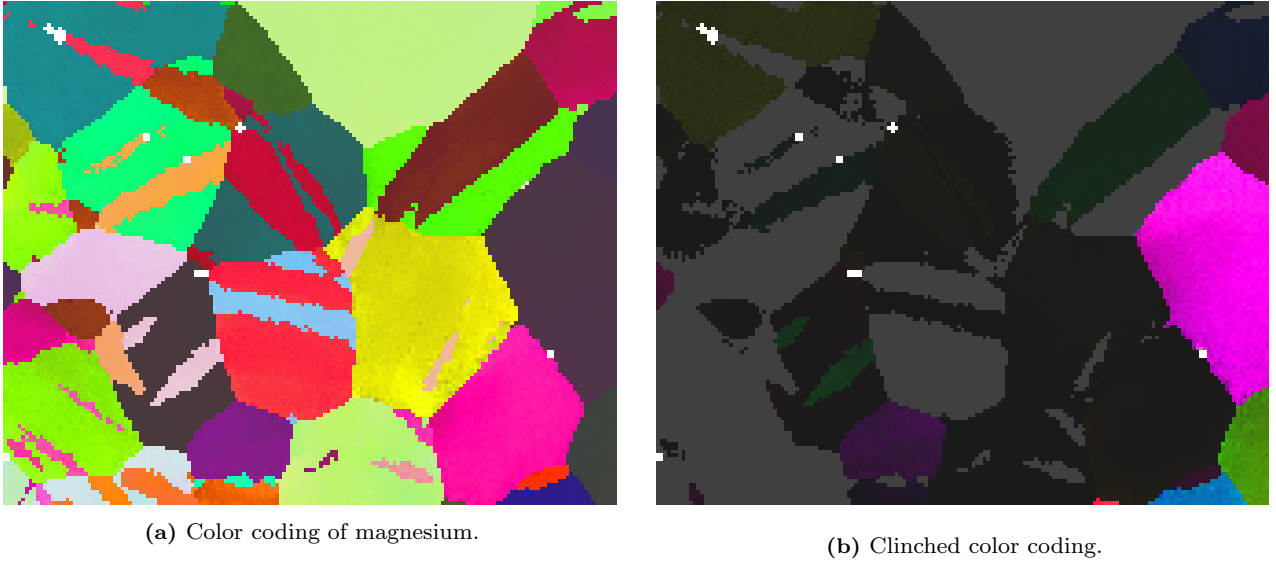


Fig. 8.6 Left: The raw EBSD data of a Magnesium sample with color visualization from [7]. Right: Clinched colorization to highlight details in single grains.

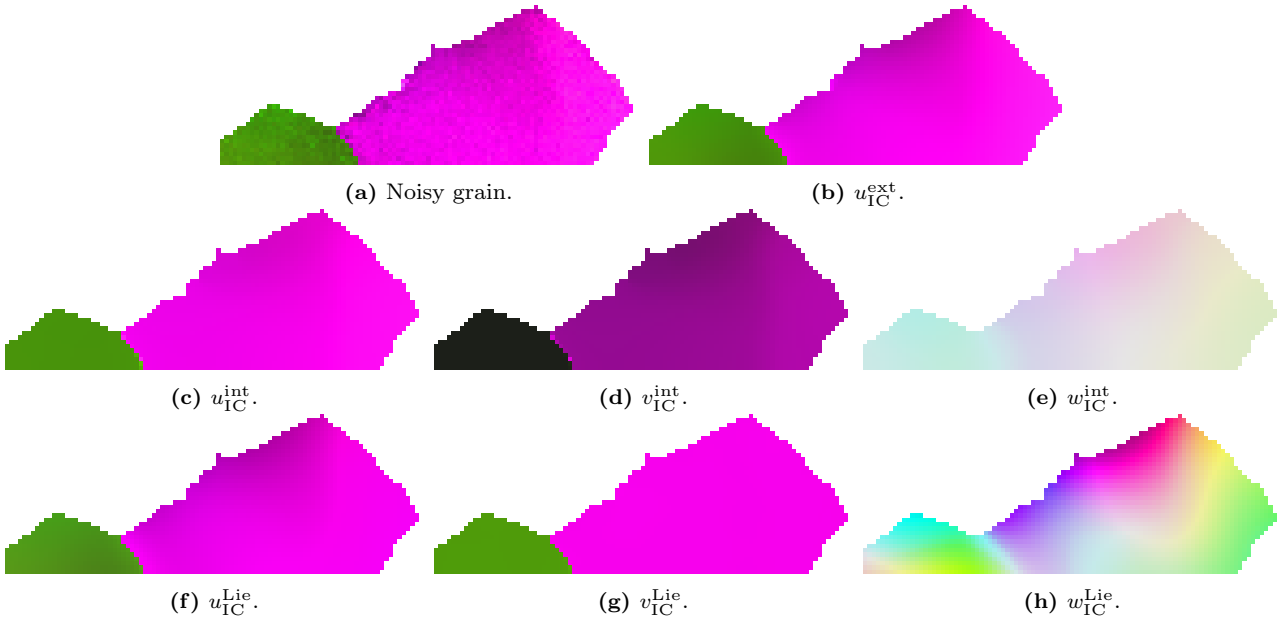


Fig. 8.7 Denoising and decomposition of EBSD data of a grain with subgrain boundary by the different IC models.

In Fig. 8.8, we apply the extrinsic and Lie group TGV model to the grain in the upper left corner of Fig. 8.6. For the extrinsic approach we chose the parameters $(\alpha = 1.4 \times 10^{-2}, \beta = \frac{3}{7})$ and for the Lie group one $(\alpha = 0.005, \beta = \frac{2}{3})$. Both methods lead to similar denoising results. However, the intrinsic Lie group TGV allows a meaningful decomposition of the “gradient”. The components of the vector $a = (a_1, a_2)$ are shown in Fig. 8.8(d) and (e). In particular, the “compensator” a_1 has a jump at the subgrain boundary.

9 Conclusions

We proposed space discrete intrinsic variational models for the restoration of manifold-valued images, where we considered three different priors, namely additive and IC coupling of absolute first and second order differences and a TGV model. For Lie groups, another approach was given based on the group operation. In contrast to our general intrinsic TGV model, where gradients and their additive components are defined in tangent spaces, the components of the TGV Lie group ap-

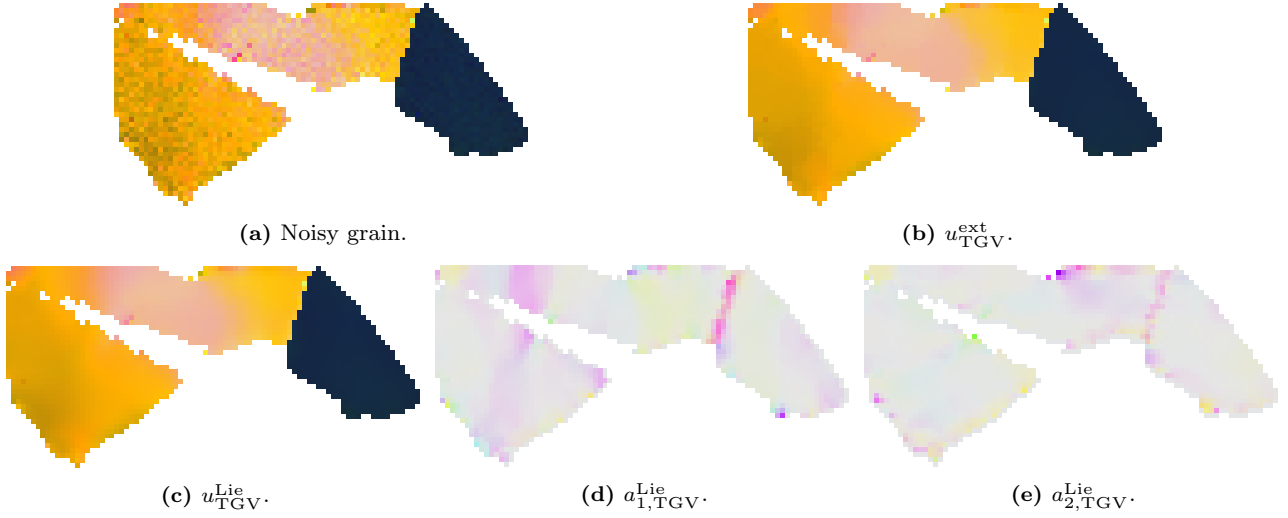


Fig. 8.8 Denoised EBSD data of a grain with subgrain boundary with the extrinsic and Lie group TGV.

proach live on the manifold. To get a better intuition of the models one should discuss what happens if the grid mesh size goes to zero. Or the other way around, a spatial continuous setting from which the current models follow by discretization is highly interesting, but clearly out of the focus of this paper. Note that for $\mathcal{M} = \mathbb{S}^1$ there exists a continuous TV approach [34,35,36].

The performance of our models was demonstrated by numerical examples. A future topic consists in speeding up the computations. In [12] we proposed for example a half-quadratic method which may be applied.

A Riemannian Gradients of Differences

Proof of Lemma 7.1: Using that the bi-invariant metric is invariant to inversion, i.e., $\text{dist}(x, y) = \text{dist}(x^{-1}, y^{-1})$ for $x, y \in \mathcal{M}$, we obtain

$$\begin{aligned} & \text{grad}_{\mathcal{M}, w_i} (d_{xy}^{\text{Lie}})^2(w_i) \\ &= \text{grad}_{\mathcal{M}, w_i} (\text{dist}^2(w_{i+(1,0)} \circ w_i^{-1}, w_{i+(1,-1)} \circ w_{i-(0,1)}^{-1})) \\ &= \text{grad}_{\mathcal{M}, w_i} (\text{dist}^2(w_i^{-1}, w_{i+(1,0)}^{-1} \circ w_{i+(1,-1)} \circ w_{i-(0,1)}^{-1})) \\ &= \text{grad}_{\mathcal{M}, w_i} (\text{dist}^2(w_i, w_{i-(0,1)} \circ w_{i+(1,-1)}^{-1} \circ w_{i+(1,0)})) \\ &= -2 \log_{w_i} (w_{i-(0,1)} \circ w_{i+(1,-1)}^{-1} \circ w_{i+(1,0)}). \end{aligned}$$

For $\xi \in T_{w_i} \mathcal{M}$ we obtain

$$\begin{aligned} & \left\langle \text{grad}_{\mathcal{M}, w_i} (d_{xx}^{\text{Lie}})^2(w_i), \xi \right\rangle_{w_i} \\ &= \left\langle \text{grad}_{\mathcal{M}, w_i} (\text{dist}^2(\cdot \circ w_{i-(1,0)}^{-1} \circ \cdot, w_{i+(1,0)})) (w_i), \xi \right\rangle_{w_i} \\ &= D(\text{dist}^2(\cdot \circ w_{i-(1,0)}^{-1} \circ \cdot, w_{i+(1,0)})) (w_i) [\xi] \\ &= D(\text{dist}^2(\cdot, w_{i+(1,0)})) (w_i \circ w_{i-(1,0)}^{-1} \circ w_i) \\ & \quad D(\cdot \circ w_{i-(1,0)}^{-1} \circ \cdot) (w_i) [\xi] \\ &= -2 \left\langle \log_{w_i \circ w_{i-(1,0)}^{-1} \circ w_i} w_{i+(1,0)}, \right. \\ & \quad \left. D(\cdot \circ w_{i-(1,0)}^{-1} \circ \cdot) (w_i) [\xi] \right\rangle_{w_i \circ w_{i-(1,0)}^{-1} \circ w_i} \end{aligned}$$

$$\begin{aligned} &= -2 \left\langle \log_{w_i \circ w_{i-(1,0)}^{-1} \circ w_i} w_{i+(1,0)}, \right. \\ & \quad \left. D\mathcal{L}_{w_i \circ w_{i-(1,0)}^{-1} \circ w_i} [\xi] + D\mathcal{R}_{w_{i-(1,0)}^{-1} \circ w_i} [\xi] \right\rangle_{w_i \circ w_{i-(1,0)}^{-1} \circ w_i} \\ &= -2 \left\langle D\mathcal{L}_{w_{i-(1,0)} \circ w_i^{-1}} [\log_{w_i \circ w_{i-(1,0)}^{-1} \circ w_i} w_{i+(1,0)}] \right. \\ & \quad \left. + D\mathcal{R}_{w_i^{-1} \circ w_{i-(1,0)}} [\log_{w_i \circ w_{i-(1,0)}^{-1} \circ w_i} w_{i+(1,0)}], \xi \right\rangle_{w_i}. \quad \square \end{aligned}$$

Proof of Lemma 7.2: First, we consider the Riemannian gradient of F_1 . As the connection is compatible with the metric, we obtain $\text{grad}_{\mathcal{M}, \xi_i} F_1$ and $\text{grad}_{\mathcal{M}, \xi_i} F_2$. For the computation of the gradients of F_1 with respect to u_i, u_{i+1} we know that the outer function has gradient T and obtain for $\zeta \in T_{u_i} \mathcal{M}$

$$\begin{aligned} D(F_1(\cdot, u_{i+1}, \xi_i))(u_i) [\zeta] &= \langle T, \tilde{L}_{u_{i+1}}(u_i) [\zeta] \rangle_{u_i} \\ &= \langle \tilde{L}_{u_{i+1}}^*(u_i) [T], \zeta \rangle_{u_i} \\ &=: \langle \text{grad}_{\mathcal{M}, u_i} \text{tv}(\cdot, u_{i+1}), \xi_i \rangle (u_i, \zeta)_{u_i}, \end{aligned}$$

Similarly we can treat the derivative with respect to u_{i+1} by replacing \tilde{L} by l . Next we handle

$$\begin{aligned} & F_2(u_i, u_{i-1}, \xi_i, \xi_{i-1}) \\ &= \|\xi_i + \log_{u_i} \left(\gamma \left(\exp_{u_{i-1}} \xi_{i-1}, \gamma(u_i, u_{i-1}; \frac{1}{2}); 2 \right) \right)\|_{u_i}^2. \end{aligned}$$

To compute the differential with respect to ξ_{i-1} we need to apply the differentials in the same order as they appear in the pole ladder. This leads for a $\zeta \in T_{u_{i-1}} \mathcal{M}$ to

$$\begin{aligned} & D(F_2(u_i, u_{i-1}, \xi_i, \cdot)) (\xi_{i-1}) [\zeta] \\ &= \left\langle S, L_{u_i}(p_i) \left[G_{\cdot, c_i, 2}(e_i) [E_{u_{i-1}}(\xi_{i-1}) [\zeta]] \right] \right\rangle_{u_i} \\ &= \left\langle E_{u_{i-1}}^*(\xi_{i-1}) \left[G_{\cdot, c_i, 2}^*(e_i) [L_{u_i}^*(p_i) [S]] \right], \zeta \right\rangle_{u_{i-1}}. \end{aligned}$$

As u_i or u_{i+1} appear twice in the pole ladder we get a sum of two differentials. For u_i appearing in the logarithm and the mid point evaluation we obtain for $\zeta \in T_{u_i} \mathcal{M}$,

$$D(F_2(\cdot, u_{i-1}, \xi_i, \xi_{i-1}))(u_i) [\zeta]$$

$$\begin{aligned}
&= \left\langle S, \tilde{L}_{p_i}(u_i)[\zeta] \right. \\
&\quad \left. + L_{u_i}(p_i) \left[G_{e_i, \cdot, 2}(c_i) \left[G_{\cdot, u_{i-1}, \frac{1}{2}}(u_i)[\zeta] \right] \right] \right\rangle_{u_i} \\
&= \left\langle \tilde{L}_{p_i}^*(u_i)[S] \right. \\
&\quad \left. + G_{\cdot, u_{i-1}, \frac{1}{2}}^*(u_i) \left[G_{e_i, \cdot, 2}^*(c_i) \left[L_{u_i}^*(p_i)[S] \right] \right], \zeta \right\rangle_{u_i}.
\end{aligned}$$

Similarly, we conclude for u_{i-1} and $\zeta \in T_{u_{i-1}}\mathcal{M}$,

$$\begin{aligned}
&D(F_2(u_i, \cdot, \xi_i, \xi_{i-1}))(u_{i-1})[\zeta] \\
&= \left\langle S, L_{u_i}(p_i) \left[G_{\cdot, c_i, 2}(e_i) \left[\tilde{E}_{\xi_{i-1}}(u_{i-1})[\zeta] \right] \right] \right. \\
&\quad \left. + L_{u_i}(p_i) \left[G_{e_i, \cdot, 2}(c_i) \left[G_{u_i, \cdot, \frac{1}{2}}(u_{i-1})[\zeta] \right] \right] \right\rangle_{u_i} \\
&= \left\langle \tilde{E}_{\xi_{i-1}}^*(u_{i-1}) \left[G_{\cdot, c_i, 2}^*(e_i) \left[L_{u_i}^*(p_i)[S] \right] \right] \right. \\
&\quad \left. + G_{u_i, \cdot, \frac{1}{2}}^*(u_{i-1}) \left[G_{e_i, \cdot, 2}^*(c_i) \left[L_{u_i}^*(p_i)[S] \right] \right], v \right\rangle_{u_i}. \quad \square
\end{aligned}$$

B Special Manifolds

B.1 The d -dimensional Sphere

Let $\mathbb{S}^d = \{x \in \mathbb{R}^{d+1} : \|x\|_2 = 1\}$ denote the d -dimensional unit sphere embedded in \mathbb{R}^{d+1} . The tangential space at $x \in \mathbb{S}^d$ is given by

$$T_x \mathbb{S}^d = \{\xi \in \mathbb{R}^{d+1} : \langle x, \xi \rangle = 0\}.$$

A Riemannian metric is the metric from the embedding space, i.e., the Euclidean inner product. The geodesic distance related to this metric is given by

$$\text{dist}(x, y) = \arccos \langle x, y \rangle,$$

where $\langle \cdot, \cdot \rangle$ is the standard scalar product in \mathbb{R}^{d+1} . The geodesic $\gamma_{x, \xi}(t)$ with $\gamma_{x, \xi}(0) = x$ and $\dot{\gamma}_{x, \xi}(0) = \xi$ is given by

$$\gamma_{x, \xi}(t) = \cos(t\|\xi\|_2)x + \sin(t\|\xi\|_2) \frac{\xi}{\|\xi\|_2}.$$

The exponential and logarithmic map read as

$$\begin{aligned}
\exp_x(\xi) &= x \cos(\|\xi\|) + \frac{\xi}{\|\xi\|} \sin(\|\xi\|), \\
\log_x(y) &= \text{dist}_{\mathbb{S}^d}(x, y) \frac{y - \langle x, y \rangle x}{\|y - \langle x, y \rangle x\|}, \quad x \neq -y.
\end{aligned}$$

The orthogonal projection of $x \in \mathbb{R}^{d+1}$ onto \mathbb{S}^d is given by $\Pi(x) = x/\|x\|_2$. The parallel transport

$$P_{x \rightarrow y} : T_x \mathbb{S}^d(r) \rightarrow T_y \mathbb{S}^d$$

along the geodesic from x to y is given by, see e.g. [42],

$$P_{x \rightarrow y}(\xi) = \xi - \frac{\langle \log_x(y), \xi \rangle}{\text{dist}_{\mathbb{S}^d}^2(x, y)} (\log_x(y) + \log_y(x)).$$

B.2 The special orthogonal group

Let $\text{SO}(3) = \{x \in \mathbb{R}^{3,3} : x^T x = I_3, \det(x) = 1\}$, be the space of rotations in \mathbb{R}^3 . The tangent space at $x \in \text{SO}(3)$ is $T_x \text{SO}(3) = x \text{Skew}(3)$, with $\text{Skew}(3) = \{x \in \mathbb{R}^{3,3} : x^T + x = 0\}$. It is a Lie group with bi-invariant metric and geodesic distance

$$\text{dist}_{\text{SO}(3)}(x, y) = \sqrt{2} \arccos \left(\frac{\text{tr}(x^T y) - 1}{2} \right).$$

An isometric representation of the rotations in \mathbb{R}^3 is given by the unit quaternions, see [38]: for $p_1, p_2 \in \mathbb{R}^4$, $p_1 = (s_1, v_1)^T$, $p_2 = (s_2, v_2)^T$, $v_1, v_2 \in \mathbb{R}^3$, the multiplication is defined by

$$p_1 \circ p_2 = \begin{pmatrix} s_1 s_2 - v_1^T v_2 \\ s_1 v_2 + s_2 v_1 + v_1 \times v_2 \end{pmatrix},$$

the unit element is $e = (1, 0, 0, 0)^T$ and the inverse is given by

$$p^{-1} = (p_1, -p_2, -p_3, -p_4).$$

A rotation of a vector $x \in \mathbb{R}^3$ around the angle $\alpha \in (0, \pi]$ and axis $r \in \mathbb{S}^2$ can be realized with

$$p(\alpha, r) := \begin{pmatrix} \cos(\frac{\alpha}{2}) \\ \sin(\frac{\alpha}{2})r \end{pmatrix}, p(\alpha, r) \circ \begin{pmatrix} 0 \\ x \end{pmatrix} \circ p(\alpha, r)^{-1} = \text{rot}(\alpha, r).$$

Note that $p(\alpha, r) \in \mathbb{S}^3$, further $p(\alpha_1, r_1) \circ p(\alpha_2, r_2) \in \mathbb{S}^3$, so the rotations can be identified with elements on the sphere \mathbb{S}^3 . As p and $-p$ yield the same rotation, we have a bijection between $\text{SO}(3)$ and $\mathbb{S}^3/\{-1, 1\}$. Furthermore $(\text{SO}(3), \text{dist}_{\text{SO}(3)})$ is isometric to $(\mathbb{S}^3/\{-1, 1\}, \sqrt{2} \text{dist}_{\mathbb{S}^3/\{-1, 1\}})$, with

$$\text{dist}_{\mathbb{S}^3/\{-1, 1\}}(p, q) = \arccos |\langle p, q \rangle|.$$

The exponential map, logarithmic map, and the projection on \mathbb{S}^3 can be used, with a few adjustments. The result of the exponential map and the projection is chosen, such that the first entry is positive. For the computation of the logarithmic map $\log_p q$, we chose the representation of q having the smallest distance to p .

B.3 Symmetric positive definite matrices

The dimension of the manifold $\mathcal{P}(r)$ of symmetric positive definite matrices is $d = \frac{r(r+1)}{2}$. Then the affine invariant geodesic distance is given by

$$\text{dist}_{\mathcal{P}(r)}(x, y) = \|\text{Log}(x^{-\frac{1}{2}} y x^{-\frac{1}{2}})\|_F,$$

where $\|\cdot\|_F$ denotes the Frobenius norm of matrices and Exp and Log denote the matrix exponential and logarithm, respectively. The tangential space at $x \in \mathcal{P}(r)$ is given by

$$T_x \mathcal{P}(r) = \{x^{\frac{1}{2}} \xi x^{\frac{1}{2}} : \xi \in \text{Sym}(r)\} = \text{Sym}(r),$$

where $\text{Sym}(r)$ denotes the space of symmetric $r \times r$ matrices. The Riemannian metric reads

$$\langle \xi_1, \xi_2 \rangle_x = \text{tr}(\xi_1 x^{-1} \xi_2 x^{-1}), \quad \xi_1, \xi_2 \in T_x \mathcal{P}(r).$$

The exponential and the logarithmic map are

$$\begin{aligned}
\exp_p(\xi) &= p^{\frac{1}{2}} \text{Exp}(p^{-\frac{1}{2}} \xi p^{-\frac{1}{2}}) p^{\frac{1}{2}}, \\
\log_p(q) &= p^{\frac{1}{2}} \text{Log}(p^{-\frac{1}{2}} q p^{-\frac{1}{2}}) p^{\frac{1}{2}}.
\end{aligned}$$

We embed the manifold of symmetric positive definite matrices $\mathcal{P}(r)$ into \mathbb{R}^n , $n = \frac{r(r+1)}{2}$, using the canonical embedding of the upper triangular matrix. Then the projection onto the closure of the manifold $\mathcal{P}(r)$ is given as follows: let $x = u\Lambda u^T$ denote the eigenvalue decomposition of an real-valued symmetric matrix $x \in \mathbb{R}^{r,r}$ represented as before by its upper triangular entries as a vector in \mathbb{R}^n . Hence u is an orthogonal matrix, and $\Lambda = \text{diag}(\lambda_1, \dots, \lambda_r)$ is the diagonal matrix of the eigenvalues of x . The projection is then given by

$$\Pi(x) = u\tilde{\Lambda}u^T, \quad \tilde{\Lambda} := \text{diag}(\tilde{\lambda}_1, \dots, \tilde{\lambda}_r), \quad \tilde{\lambda}_i := \max\{0, \lambda_i\}.$$

The parallel transport

$$P_{x \rightarrow y}: T_x \mathcal{P}(r) \rightarrow T_y \mathcal{P}(r)$$

along the geodesic from x to y is given by

$$P_{x \rightarrow y}(\xi) = \gamma_{x,y}(\tfrac{1}{2})x^{-1}\xi x^{-1}\gamma_{x,y}(\tfrac{1}{2}).$$

Acknowledgements R. Bergmann wants to thank B. Wirth (University of Münster) for fruitful discussions on Schild's ladder TGV. Funding by the German Research Foundation (DFG) within the project STE 571/13-1 & BE 5888/2-1 and within the Research Training Group 1932, project area P3, is gratefully acknowledged.

References

1. P.-A. Absil, R. Mahony, and R. Sepulchre. *Optimization Algorithms on Matrix Manifolds*. Princeton University Press, Princeton and Oxford, 2008.
2. F. Alouges. A new algorithm for computing liquid crystal stable configurations: The harmonic mapping case. *SIAM Journal on Numerical Analysis*, 34(5):1708–1726, 1997.
3. V. Arsigny, X. Pennec, and N. Ayache. Bi-invariant means in Lie groups. application to left-invariant polyaffine transformations. *HAL Preprint*, 00071383, 2006.
4. H. Attouch, J. Bolte, and B. F. Svaiter. Convergence of descent methods for semi-algebraic and tame problems: proximal algorithms, forward-backward splitting, and regularized Gauss-Seidel methods. *Mathematical Programming*, 137(1):91–129, 2013.
5. M. Bačák. *Convex analysis and optimization in Hadamard spaces*, volume 22 of *De Gruyter Series in Nonlinear Analysis and Applications*. De Gruyter, Berlin, 2014.
6. M. Bačák, R. Bergmann, G. Steidl, and A. Weinmann. A second order non-smooth variational model for restoring manifold-valued images. *SIAM Journal on Scientific Computing*, 38(1):A567–A597, 2016.
7. F. Bachmann and R. Hielscher. MTEX – MATLAB toolbox for quantitative texture analysis. <http://mtex-toolbox.github.io/>, 2005–2016.
8. F. Bachmann, R. Hielscher, P. E. Jupp, W. Pantleon, H. Schaeben, and E. Wegert. Inferential statistics of electron backscatter diffraction data from within individual crystalline grains. *Journal of Applied Crystallography*, 43:1338–1355, 2010.
9. F. Balle, T. Beck, D. Eifler, J. H. Fitschen, S. Schuff, and G. Steidl. Strain analysis by a total generalized variation regularized optical flow model. *Inverse Problems in Science & Engineering*, 2017. accepted with minor revision.
10. F. Balle, D. Eifler, J. H. Fitschen, S. Schuff, and G. Steidl. Computation and visualization of local deformation for multiphase metallic materials by infimal convolution of TV-type functionals. In *SSVM 2015, Lecture Notes in Computer Science*, pages 385–396. Springer, 2015.
11. R. Bamler and P. Hartl. Synthetic aperture radar interferometry. *Inverse Problems*, 14(4):R1–R54, 1998.
12. R. Bergmann, R. H. Chan, R. Hielscher, J. Persch, and G. Steidl. Restoration of manifold-valued images by half-quadratic minimization. *Inverse Problems and Imaging*, 10(2):281–304, 2016.
13. R. Bergmann, J. H. Fitschen, J. Persch, and G. Steidl. Infimal convolution coupling of first and second order differences on manifold-valued images. In F. Lauze, Y. Dong, and A. B. Dahl, editors, *Scale Space and Variational Methods in Computer Vision: 6th International Conference, SSVM 2017, Kolding, Denmark, June 4-8, 2017, Proceedings*, pages 447–459. Springer International Publishing, Cham, 2017.
14. R. Bergmann, F. Laus, G. Steidl, and A. Weinmann. Second order differences of cyclic data and applications in variational denoising. *SIAM Journal on Imaging Sciences*, 7(4):2916–2953, 2014.
15. R. Bergmann and D. Tenbrinck. A graph framework for manifold-valued data. *arXiv Preprint 1702.05293*, 2017.
16. R. Bergmann and A. Weinmann. Inpainting of cyclic data using first and second order differences. In *Energy Minimization Methods in Computer Vision and Pattern Recognition*, pages 155–168. Springer, 2015.
17. R. Bergmann and A. Weinmann. A second order TV-type approach for inpainting and denoising higher dimensional combined cyclic and vector space data. *Journal of Mathematical Imaging and Vision*, 55(3):401–427, 2016.
18. K. Bredies. Recovering piecewise smooth multichannel images by minimization of convex functionals with total generalized variation penalty. In A. Bruhn, T. Pock, and X.-C. Tai, editors, *Efficient Algorithms for Global Optimization Methods in Computer Vision*, pages 44–77. Springer, 2014.
19. K. Bredies and M. Holler. Regularization of linear inverse problems with total generalized variation. *Journal of Inverse and Ill-posed Problems*, 22(6):871–913, 2014.
20. K. Bredies, M. Holler, M. Storath, and A. Weinmann. Total generalized variation for manifold-valued data. *Preprint arXiv:1709.01616*, 2017.
21. K. Bredies, K. Kunisch, and T. Pock. Total generalized variation. *SIAM Journal on Imaging Sciences*, 3(3):492–526, 2010.
22. K. Bredies and H. P. Sun. Preconditioned Douglas-Rachford algorithms for TV- and TGV-regularized variational imaging problems. *Journal of Mathematical Imaging and Vision*, 52(3):317–344, Jul 2015.
23. K. Bredies and T. Valkonen. Inverse problems with second-order total generalized variation constraints. In *International Conference on Sampling Theory and Applications*, 2011.
24. M. Burger, A. Sawatzky, and G. Steidl. First order algorithms in variational image processing. In R. Glowinski, S. Osher, and W. Yin, editors, *Operator Splittings and Alternating Direction Methods*. Springer, 2016.
25. R. Bürgmann, P. A. Rosen, and E. J. Fielding. Synthetic aperture radar interferometry to measure earth's surface topography and its deformation. *Annu. Rev. Earth Planet. Sci.*, 28(1):169–209, 2000.
26. A. Chambolle and P.-L. Lions. Image recovery via total variation minimization and related problems. *Numerische Mathematik*, 76(2):167–188, 1997.

27. D. Cremers and E. Strelakovsky. Total cyclic variation and generalizations. *Journal of Mathematical Imaging and Vision*, 47(3):258–277, 2013.
28. M. P. do Carmo. *Riemannian Geometry*, volume 115. Birkhäuser, Basel, 1992. Translated by F. Flatherty.
29. J. Ehlers, F. A. E. Pirani, and A. Schild. The geometry of free fall and light propagation. In L. O’Reifeartaigh, editor, *General Relativity*, pages 63–84. Oxford University Press, 1972.
30. J. H. Fitschen. *Variational Models in Image Processing with Applications in the Materials Sciences*. Dissertation, University of Kaiserslautern, 2017. Similarly: Verlag Dr. Hut, ISBN 978-3843932455, 2017.
31. P. Fletcher and S. Joshi. Riemannian geometry for the statistical analysis of diffusion tensor data. *Signal Processing*, 87:250–262, 2007.
32. D. Gabay and B. Mercier. A dual algorithm for the solution of nonlinear variational problems via finite element approximations. *Computer and Mathematics with Applications*, 2:17–40, 1976.
33. J. Gallier and J. Quaintance. Notes on Differential Geometry and Lie Groups, 2017.
34. M. Giaquinta, G. Modica, and J. Souček. Variational problems for maps of bounded variation with values in S^1 . *Calculus of Variation*, 1(1):87–121, 1993.
35. M. Giaquinta and D. Mucci. The BV-energy of maps into a manifold: relaxation and density results. *Ann. Sc. Norm. Super. Pisa Cl. Sci.*, 5(4):483–548, 2006.
36. M. Giaquinta and D. Mucci. Maps of bounded variation with values into a manifold: total variation and relaxed energy. *Pure and Applied Mathematics Quarterly*, 3(2):513–538, 2007.
37. R. Glowinski and A. Marroco. Sur l’approximation, par éléments finis d’ordre un, et la résolution, par pénalisation-dualité d’une classe de problèmes de Dirichlet non linéaires. *Revue française d’automatique, informatique, recherche opérationnelle. Analyse numérique*, 9(2):41–76, 1975.
38. M. Gräf. A unified approach to scattered data approximation on S^3 and $SO(3)$. *Advances in Computational Mathematics*, 37(3):379–392, 2012.
39. V. K. Gupta and S. R. Agnew. A simple algorithm to eliminate ambiguities in ebsd orientation map visualization and analyses: Application to fatigue crack-tips/wakes in aluminum alloys. *Microscopy and Microanalysis*, 16:831, 2010.
40. M. Holler and K. Kunisch. On infimal convolution of TV-type functionals and applications to video and image reconstruction. *SIAM Journal on Imaging Sciences*, 7(4):2258–2300, 2014.
41. H. Hopf and W. Rinow. Ueber den begriff der vollständigen differentialgeometrischen fläche. *Commentarii Mathematici Helvetici*, 3(1):209–225, Dec 1931.
42. S. Hosseini and A. Uschmajew. A Riemannian gradient sampling algorithm for nonsmooth optimization on manifolds. *SIAM Journal on Optimization*, 27(1):173–189, 2017.
43. F. Jarre. Convex analysis on symmetric matrices. In H. Wolkowicz, R. Saigal, and L. Vandenbergh, editors, *Handbook of Semidefinite Programming*. Kluwer Academic Publishers, 2000.
44. A. Kheyfets, W. A. Miller, and G. A. Newton. Schild’s ladder parallel transport procedure for an arbitrary connection. *International Journal of Theoretical Physics*, 39(12):2891–2898, Dec 2000.
45. F. Laus, M. Nikolova, J. Persch, and G. Steidl. A nonlocal denoising algorithm for manifold-valued images using second order statistics. *SIAM Journal on Imaging Sciences*, 10(1):416–448, March 2017.
46. J. Lellmann, E. Strelakovsky, S. Koetter, and D. Cremers. Total variation regularization for functions with values in a manifold. In *IEEE ICCV 2013*, pages 2944–2951, 2013.
47. G. Li and T. K. Pong. Global convergence of splitting methods for nonconvex composite optimization. *Preprint arXiv: 1407.0753*, 753, 2014.
48. M. Lorenzi and X. Pennec. Efficient parallel transport of deformations in time series of images: From Schild’s to pole ladder. *Journal of Mathematical Imaging and Vision*, 50(1):5–17, Sep 2014.
49. J. Nash. The imbedding problem for Riemannian manifolds. *Annals of Mathematics*, 63(1):20–63, 1956.
50. K. Papafitsoros and C. B. Schönlieb. A combined first and second order variational approach for image reconstruction. *Journal of Mathematical Imaging and Vision*, 2(48):308–338, 2014.
51. X. Pennec. Pole ladder: an exact scheme for parallel transport in symmetric spaces. *In preparation*, 2018.
52. J. Persch. Optimization methods in manifold-valued image processing. *PhD Thesis, TU Kaiserslautern*, 2018.
53. Q. Rentmeesters. A gradient method for geodesic data fitting on some symmetric Riemannian manifolds. In *50th IEEE Conference on Decision and Control and European Control Conference 2011*, pages 7141–7146, 2011.
54. R. T. Rockafellar. *Convex Analysis*. Princeton University Press, 1970.
55. G. Rosman, X.-C. Tai, R. Kimmel, and A. M. Bruckstein. Augmented-Lagrangian regularization of matrix-valued maps. *Methods and Applications of Analysis*, 21(1):121–138, 2014.
56. G. Rosman, Y. Wang, X.-C. Tai, R. Kimmel, and A. M. Bruckstein. Fast regularization of matrix-valued images. In *Efficient Algorithms for Global Optimization Methods in Computer Vision*, pages 19–43. Springer, 2014.
57. W. Rossmann. *Lie Groups*. Oxford Science Publications, Oxford, 2003.
58. L. I. Rudin, S. Osher, and E. Fatemi. Nonlinear total variation based noise removal algorithms. *Physica D: Nonlinear Phenomena*, 60(1):259–268, 1992.
59. S. Sasaki. On the differential geometry of tangent bundles of Riemannian manifolds. *Tohoku Mathematical Journal, Second Series*, 10(3):338–354, 1958.
60. S. Setzer and G. Steidl. Variational methods with higher order derivatives in image processing. In *Approximation XII: San Antonio 2007*, pages 360–385, 2008.
61. S. Setzer, G. Steidl, and T. Teuber. Infimal convolution regularizations with discrete ℓ_1 -type functionals. *Communications in Mathematical Sciences*, 9(3):797–827, 2011.
62. G. Steidl, S. Setzer, B. Popilka, and B. Burgeth. Restoration of matrix fields by second order cone programming. *Computing*, 81:161–178, 2007.
63. E. Strelakovsky and D. Cremers. Total variation for cyclic structures: convex relaxation and efficient minimization. In *2011 IEEE Conference on Computer Vision and Pattern Recognition (CVPR)*, pages 1905–1911, 2011.
64. S. Sun, B. Adams, and W. King. Observation of lattice curvature near the interface of a deformed aluminium bicrystal. *Phil. Mag. A*, 80:9–25, 2000.
65. T. Valkonen, K. Bredies, and F. Knoll. Total generalized variation in diffusion tensor imaging. *SIAM Journal on Imaging Sciences*, 6(1):487–525, 2013.
66. Y. Wang, W. Yin, and J. Zeng. Global convergence of ADMM in nonconvex nonsmooth optimization. *ArXiv preprint 1511.06324*, 2015.

-
67. A. Weinmann, L. Demaret, and M. Storath. Total variation regularization for manifold-valued data. *SIAM Journal on Imaging Sciences*, 7(4):2226–2257, 2014.
 68. H. Whitney. Differentiable manifolds. *Annals of Mathematics*, 37(3):645–680, 1936.